Tietze, K., Ritter, O. (2013): 3D magnetotelluric inversion in practice - the electrical conductivity structure of the San Andreas Fault in Central California. - Geophysical Journal International, 195, 1, pp. 130—147.

DOI: http://doi.org/10.1093/gji/ggt234

Geophysical Journal International

Geophys. J. Int. (2013) **195,** 130–147
Advance Access publication 2013 July 4

doi: 10.1093/gji/ggt234

Three-dimensional magnetotelluric inversion in practice—the electrical conductivity structure of the San Andreas Fault in Central California

Kristina Tietze and Oliver Ritter

Helmholtz Centre Potsdam, German Research Centre for Geosciences—GFZ, Potsdam, Germany. E-mail: ktietze@gfz-potsdam.de

Accepted 2013 June 10. Received 2013 April 29; in original form 2012 February 22

SUMMARY

3-D inversion techniques have become a widely used tool in magnetotelluric (MT) data interpretation. However, with real data sets, many of the controlling factors for the outcome of 3-D inversion are little explored, such as alignment of the coordinate system, handling and influence of data errors and model regularization. Here we present 3-D inversion results of 169 MT sites from the central San Andreas Fault in California. Previous extensive 2-D inversion and 3-D forward modelling of the data set revealed significant along-strike variation of the electrical conductivity structure. 3-D inversion can recover these features but only if the inversion parameters are tuned in accordance with the particularities of the data set.

Based on synthetic 3-D data we explore the model space and test the impacts of a wide range of inversion settings. The tests showed that the recovery of a pronounced regional 2-D structure in inversion of the complete impedance tensor depends on the coordinate system. As interdependencies between data components are not considered in standard 3-D MT inversion codes, 2-D subsurface structures can vanish if data are not aligned with the regional strike direction. *A priori* models and data weighting, that is, how strongly individual components of the impedance tensor and/or vertical magnetic field transfer functions dominate the solution, are crucial controls for the outcome of 3-D inversion. If deviations from a prior model are heavily penalized, regularization is prone to result in erroneous and misleading 3-D inversion models, particularly in the presence of strong conductivity contrasts. A 'good' overall rms misfit is often meaningless or misleading as a huge range of 3-D inversion results exist, all with similarly 'acceptable' misfits but producing significantly differing images of the conductivity structures. Reliable and meaningful 3-D inversion models can only be recovered if data misfit is assessed systematically in the frequency–space domain.

Key words: Inverse theory; Magnetotelluric; Geomagnetic induction; Continental margins: transform; Crustal structure; North America.

1 INTRODUCTION

With advancing computational resources, 3-D inversion techniques have become practical in recent years and are now a more widely used tool for magnetotelluric (MT) data interpretation. A number of 3-D inversion programs using various approaches for both forward modelling and inversion have been developed (e.g. Newman & Alumbaugh 2000; Zhdanov *et al.* 2000; Mackie *et al.* 2001; Sasaki 2001; Farquharson *et al.* 2002; Siripunvaraporn *et al.* 2005; Han *et al.* 2008; Avdeev & Avdeeva 2009; Siripunvaraporn & Egbert 2009; Egbert & Kelbert 2012). However, full 3-D inversion still is very challenging numerically and practically. Typical data sets of modern regional MT studies consist of many irregularly spaced sites, affected by noise and the inversion problem is strongly ill-posed and non-unique.

Many of the existing 3-D MT studies focus on local geological features with model grids spanning up to a few tens of square kilometres for investigations of geothermal areas and/or small volcanic complexes (Heise *et al.* 2008; Newman *et al.* 2008; Ingham *et al.* 2009; Árnason *et al.* 2010; Cumming & Mackie 2010), ore deposits (Tuncer *et al.* 2006; Farquharson & Craven 2009; Xiao *et al.* 2010) and hydrocarbon reservoirs (He *et al.* 2010). These targets represent spatially limited structures, which usually have a fairly good station coverage compared to model mesh sizes. Other surveys concentrate on investigating terrane-scale tectonic structures, for example, extended volcanic complexes (Hill *et al.* 2009; Kelbert *et al.* 2012) and major fault systems (Meqbel 2009), or a series of major geological units (Patro & Egbert 2008; Türkoğlu *et al.* 2009; Heise *et al.* 2010; Zhdanov *et al.* 2010; Patro & Egbert 2011; Bertrand *et al.* 2012a,b).

The above-mentioned MT studies are based on measurements sampled at 19 (Xiao *et al.* 2010) and up to 220 (Heise *et al.* 2010) sites and spanning a period range of 2–4 decades. Most of these data sets provide an areal station distribution, but Bertrand *et al.* (2012b), Meqbel (2009), Patro & Egbert (2011) and Xiao *et al.* (2010) worked with data from single, two intersecting and two parallel profiles, respectively. In 3-D environments, all four complex components of the impedance tensor (Z) contain information about the subsurface. Newman *et al.* (2008), Tuncer *et al.* (2006) and Zhdanov *et al.* (2010) used only the off-diagonal tensor elements for their inversions. Newman *et al.* (2008) found, that integrating Zxx and Zyy into the data set degrades the performance of the inversion due to the lower magnitudes and, therefore, lower signal-to-noise ratios of these elements. Patro & Egbert (2011) compare full-tensor inversion models with results from off-diagonal impedances and magnetic transfer functions only. Recently, first results from joint inversion of impedances and magnetic transfer functions of field data have been presented by Kelbert *et al.* (2012).

In 3-D inversion, transfer function estimates are often directly taken as input without making assumptions regarding strike directions or coordinate systems. In 3-D data sets, the 2×2 impedance tensor is fully occupied; electric and magnetic fields are elliptically polarized and non-orthogonal (Becken *et al.* 2008a). Within a complex 3-D medium, the polarization directions of both fields and their relative orientation change laterally and with depth. Hence, the information on the subsurface is usually distributed over all tensor elements and the impedance tensor cannot be split up into independent components by rotation such as the 2-D TE and TM modes. The underlying coordinate system matters, however, if only a subset of the impedance tensor is inverted. Árnason *et al.* (2010), Bertrand *et al.* (2012a) and Patro & Egbert (2011) present inversion results with data and model grid rotated to the predominant geological strike direction of the survey area. Árnason *et al.* (2010) argue that this facilitates a better resolution of the subsurface.

Data errors are also handled very differently by various authors. Árnason *et al.* (2010), Farquharson & Craven (2009) and Patro & Egbert (2008) use the statistically determined variances of the impedance tensor elements; other authors combine impedance variances with pre-set error floors (Tuncer *et al.* 2006; Ingham *et al.* 2009; Meqbel 2009; Türkoğlu *et al.* 2009; Patro & Egbert 2011; Bertrand *et al.* 2012a), or use relative error bounds (i.e. a percentage of the data value) (Heise *et al.* 2008, 2010; Newman *et al.* 2008; Hill *et al.* 2009; He *et al.* 2010; Xiao *et al.* 2010).

Model validation or appraisal includes (i) using only subsets of observation sites (Ingham *et al.* 2009) and period ranges (Newman *et al.* 2008; Farquharson & Craven 2009), (ii) varying regularization (smoothing) parameters (Patro & Egbert 2008, 2011; Heise *et al.* 2010), (iii) forward modelling sensitivity tests for particular (isolated) features of the inversion result (Hill *et al.* 2009; Xiao *et al.* 2010; Bertrand *et al.* 2012a; Kelbert *et al.* 2012) or comparison of 3-D forward modelling of principle model structures (Tuncer *et al.* 2006; Heise *et al.* 2008; Meqbel 2009). In addition, a considerable number of 3-D models have been examined in view of 2-D inversion results, based on subsets of data (Tuncer *et al.* 2006; Newman *et al.* 2008; Farquharson & Craven 2009; Hill *et al.* 2009; Ingham *et al.* 2009; Türkoğlu *et al.* 2009; Cumming & Mackie 2010; He *et al.* 2010; Heise *et al.* 2010; Bertrand *et al.* 2012a), particularly for data sets recorded along profiles (Meqbel 2009; Patro & Egbert 2011; Bertrand *et al.* 2012b). Most authors found the main structural features of 2-D and 3-D modelling results in good agreement, provided the data were prepared appropriately for 2-D modelling. However, other studies revealed significant differences between 2-D and 3-D results, which are usually attributed to the limitations of the 2-D interpretation (e.g. Meqbel 2009; Heise *et al.* 2010; Patro & Egbert 2011).

The main interest of the study presented here, is to better understand 3-D effects in the data and 3-D inversion of real MT data in practice. For 3-D inversion and forward modelling the ModEM package of Egbert & Kelbert (2012) was used. The inversion algorithm is based on a standard minimum-structure non-linear conjugate gradients algorithm. The program is parallelized to enable concurrent computations of different frequencies and source polarizations (Meqbel 2009).

A range of inversion parameters and settings can severely influence the outcome of the final inversion results. Parameters tested include the orientation of the inversion coordinate system, the influence of data error bounds (i.e. data weighting), and model regularization parameters (smoothing and prior model). We use synthetic modelling to emulate principal features revealed by 2-D and 3-D inversion of the field data to test if and how well such features can be recovered by 3-D inversion.

2 THE DATA SET FROM CALIFORNIA

The MT data set considered here comprises measurements at more than 250 sites recorded along seven profiles between 2005 and 2008 (see Fig. 1). The survey area extends by 70 km $\times$ 130 km in the vicinity of the San Andreas Fault Observatory at Depth (SAFOD) covering the transitional segment of the San Andreas Fault (SAF) where the fault changes its behaviour from creeping to being locked, and where a source area of non-volcanic tremors has been located (Nadeau & Dolenc 2005; Shelly *et al.* 2009; Ryberg *et al.* 2010; Shelly 2010; Shelly & Hardebeck 2010; Zhang *et al.* 2010). The profile separation is roughly 10 km, the site spacing along the profiles varies from 0.5 km in the central parts across the SAF to approximately 10 km towards the profile ends.

Data were acquired at all sites in the period range from 0.01 to 1000 s with non-polarisable Ag/AgCl electrodes from GFZ Potsdam and Metronix MFS 05/06 induction-coil magnetometers. In addition, 120 of these sites were equipped with Geomagnet fluxgate magnetometers and operated for up to 5 weeks, extending the period range to more than 20 000 s. MT transfer functions were calculated using robust single site and remote reference processing routines (Egbert & Booker 1986; Egbert 1997; Ritter *et al.* 1998; Weckmann *et al.* 2005) and applying delay filtering techniques to the original time-series in order to eliminate periodic cultural noise (Becken *et al.* 2008b, 2011). The quality of the transfer functions is generally high for the entire array and all periods.

In preparation for 3-D inversion, the impedance tensor elements and vertical magnetic transfer functions (VTFs) were smoothed using a spline function and interpolated to 18 periods distributed evenly on a logarithmic scale in the range between 0.08 and 11 000 s. Data subsequently underwent manual inspection and data points deviating significantly from the original curves were excluded from the data set. To set up the data set for 3-D inversion, MT sites were selected to obtain a uniform site spacing of approximately 2 km in the densely sampled areas. We generally prefer sites with high data quality, covering a wide period range and/or where both impedances and VTFs are available. The final data set consists of 169 sites (red + white circles in Fig. 1). In addition, a 73-site subset was defined, which provides a more uniform site spacing of approximately 10 km over the entire array (red circles).

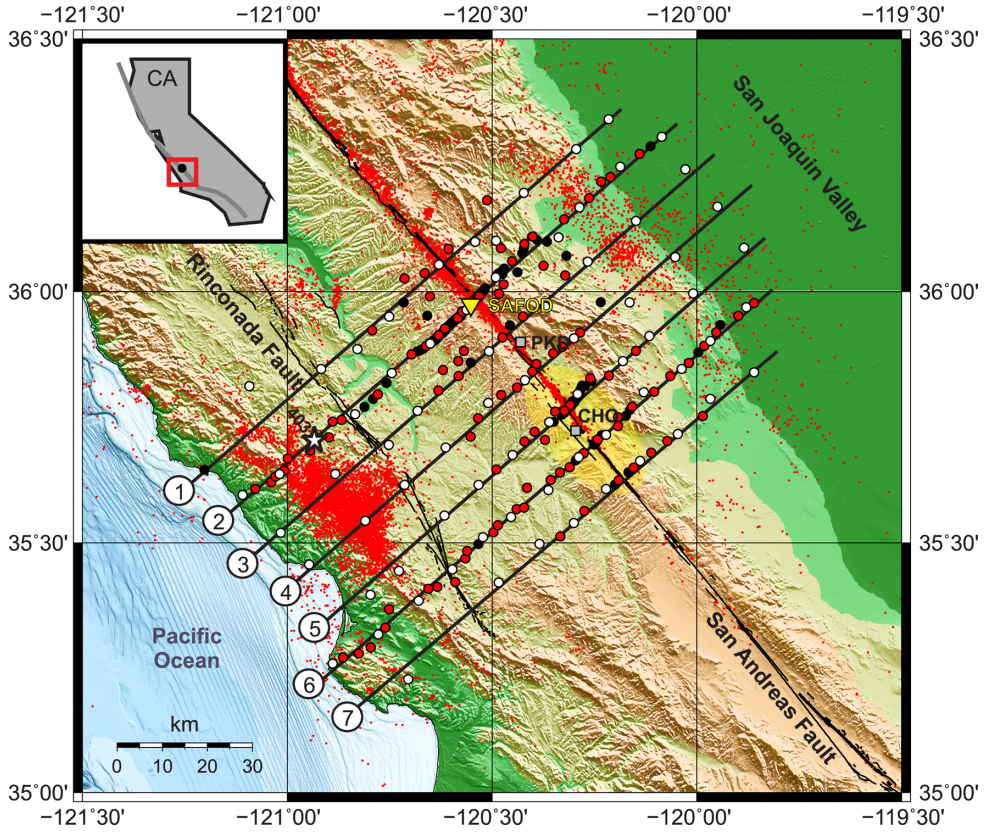

Figure 1. More than 250 MT sites were deployed along seven profiles across the San Andreas Fault in the vicinity of Parkfield and Cholame in California, USA. The sites marked by circles cover an area of 130 km × 70 km. For 3-D inversion two data subsets comprising 73 sites (white circles) and 169 sites (white + red circles) were used (see text). The asterisk marks site 403. The location of the San Andreas Fault Observatory at Depth (SAFOD) is indicated by a yellow triangle. Small red dots indicate seismicity (NCDEC 2002–2011, $M > 1.0$), the yellow shaded area outlines the main cluster of non-volcanic tremors after Zhang *et al.* (2010). CHO, Cholame; PKD, Parkfield.

The data set exhibits a predominant geo-electric strike direction of N41°W (Becken *et al.* 2011), which is consistent with the strike direction of the regional geology (Page *et al.* 1998). However, significant influence of 3-D subsurface structures on the data set is indicated by the large number of data points where the phase tensor (PT) beta criterion (Caldwell *et al.* 2004) significantly deviates from zero (Fig. 2). For the 169-site data set, PT beta values exceed ±1° at 50 per cent and ±3° at 25 per cent of the data points. The impact of 3-D structures is most pronounced in the period range between 10 and 2000 s.

3 PRELIMINARY CONSIDERATIONS FOR 3-D INVERSION

Initially, we performed a series of 3-D inversion tests to identify an optimal inversion set-up. To minimize influences of irregular site spacing, we used the subset of 73 sites (see above).

ModEM3DMT employs a Cartesian, right-handed coordinate system with z pointing positive downwards. Data have to be rotated to align with the inversion coordinate system. For the California MT array, we tested inversion coordinate systems with the x-axis aligned (i) with geographic north (N00°) and (ii) with the geo-electric strike (N41°W).

For the N00° inversion set-up, the corresponding model grid consists of 77 × 77 × 57 cells in the two horizontal and vertical directions, respectively. The inner part comprises a uniform mesh of 35 × 35 × 57 cells with an edge length of 4.0 km. On all four sides, the central domain is padded with 21 planes where cell sizes increase laterally by a factor of 1.3. The vertical thickness is 25 m for the first layer; subsequent layer thicknesses successively increase by a factor of 1.2. For the strike-aligned inversion set-up, fewer cells are required as the grid is better aligned with the station layout (*cf.* Fig. 1). The strike-aligned model mesh comprises 20 × 40 × 57 cells in the central domain using a horizontal discretization of 4 km × 4 km. On all four sides, the central domain is padded by 15 planes, where cell sizes increase laterally by a factor of 1.3. The vertical discretization is the same as for the N00° mesh.

Within the inversion process, the ModEM3DMT algorithm seeks to minimize the penalty function Ψ, which consists of a data regularization and a model regularization term (Egbert & Kelbert 2012):

$$\Psi(\mathbf{m},\mathbf{d}) = (\mathbf{d}-\mathbf{f}(\mathbf{m}))^{\mathrm{T}}\,\mathbf{C}_d^{-1}\,(\mathbf{d}-\mathbf{f}(\mathbf{m})) + \lambda\left(\mathbf{m}-\mathbf{m}_{\mathrm{prior}}\right)^{\mathrm{T}}\mathbf{C}_m^{-1}\left(\mathbf{m}-\mathbf{m}_{\mathrm{prior}}\right), \quad (1)$$

where $\mathbf{d}$ is the observed data, $\mathbf{m}$ the conductivity model, $\mathbf{f}(\mathbf{m})$ the forward response, $\mathbf{C}_d$ the data covariance, $\mathbf{m}_{\mathrm{prior}}$ the prior model, $\mathbf{C}_m$ the model covariance and λ a trade-off parameter. The data covariance is a diagonal matrix, which contains the inverse of the squared data errors $\mathbf{e}_i$ for each data point: $\mathbf{C}_d = \mathrm{diag}(1/e_i^2)$. The model covariance $\mathbf{C}_m$ is a 3-D smoothing and scaling operator, similar to the scheme of Siripunvaraporn & Egbert (2000). $\mathbf{C}_m$ is applied to the distance of the current model $\mathbf{m}$ to the *a priori* model $\mathbf{m}_{\mathrm{prior}}$; in other words, ModEM3DMT penalizes smoothed deviations from a prior model as part of the model update search. Hence, prior model properties and smoothing parameter settings

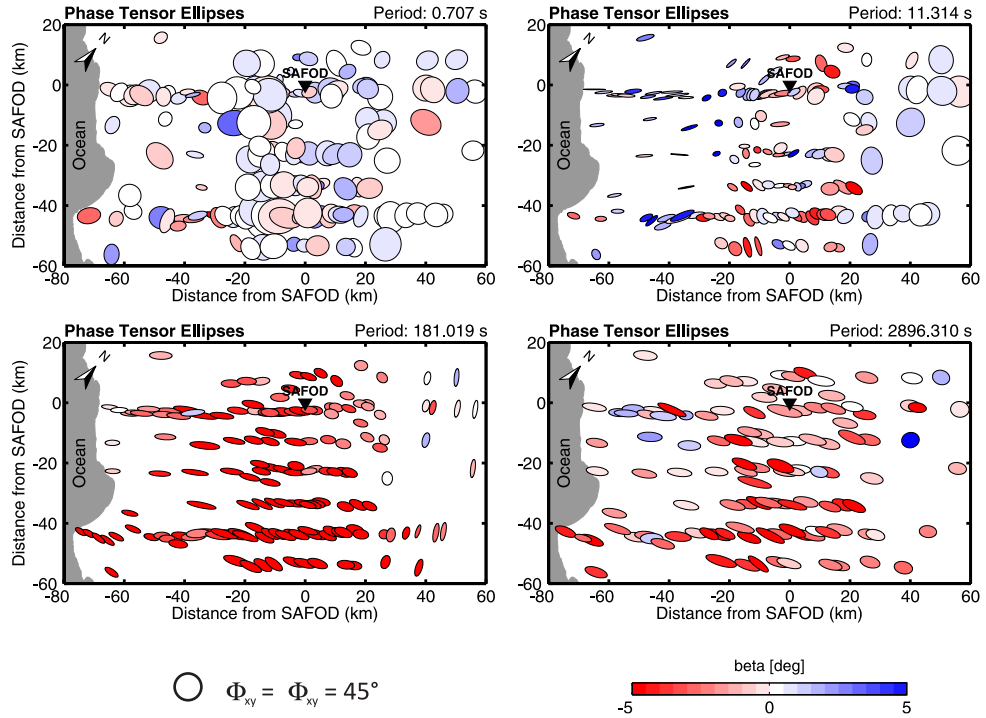

Figure 2. Phase tensor ellipses for periods of 0.71, 11.3, 181 and 2896 s. Beta values significantly deviating from zero (red and blue colouring) indicate influences of a 3-D subsurface for periods >1 s. The orientation of phase tensor ellipses is consistent with a strike direction of N41°W.

are closely interrelated. In addition, the inversion tends to keep or return to the assumed prior resistivities where the model is poorly constrained. Here, we concentrate more on the influence of the prior model resistivity structure; a comprehensive investigation of smoothing scale lengths is beyond the scope of this paper. Overall, the model regularization scheme of ModEM3DMT is similar to what is used in WSINV3DMT (Siripunvaraporn *et al.* 2005).

For all field data inversions, a coarse 3-D bathymetry of the Pacific Ocean was included as *a priori* information. A resistivity of 0.3 Ωm was assigned to the sea water and this model domain was kept fixed at all times during the inversion. We set the remaining 'land cells' to 10 Ωm and prior and starting models were always identical. For the N00° set-up, we used horizontally isotropic model smoothing; for the N41°W set-up smoothing was increased parallel to strike.

For a first overview, we inverted impedance and VTF data both jointly and separately for each coordinate set-up. Measured data errors were discarded in favour of relative error bounds. Impedance error bounds were set to 5 and 3 per cent of $|Zij|$ for diagonal and off-diagonal impedance tensor elements, in combination with a floor of 3 per cent of $|Zxy * Zyx|^{1/2}$ for the diagonal elements. For the VTF we used constant error bounds of 0.02. The 3-D inversion results are summarized in Fig. 3.

The uppermost 10 km comprise low resistivities (<10 Ωm), with thicknesses of 1–3 km for most parts of the array, which reach up to approximately 9 km in the San Joaquin valley in the SW. For greater depths, however, the inversion results are strikingly different. The joint impedance + VTF and impedance-only inversions in the N00° set-up (Figs 3a and b) are dominated by wide-stretching zones of uniformly high resistivities. Values range from 100 to 500 Ωm on the inland side of the SAF; on the Pacific side resistivities exceed 500 Ωm reaching up to 2000 Ωm. In contrast, resistivity models recovered for the strike-aligned set-up (Figs 3d and e) image an extended, highly conductive zone (HCZ, 1–10 Ωm) within the Pacific Plate. The HCZ is located approximately 30 km southwest of the surface trace of the SAF at about 15–25 km depth and extends for approximately 100 km parallel to strike.

3-D inversion for VTFs, however, yields very similar resistivity structures for both coordinate set-ups, which also contain a HCZ at depth (Figs 3c and f). Overall, both models show relatively conductive deeper subsurface as VTF-only data cannot resolve absolute resistivity levels. The inversion results are biased towards the low prior model resistivity (10 Ωm). The sedimentary cover, however, appears similarly to the impedance results, suggesting that a prior resistivity of 10 Ωm is a reasonable assumption for the shallow resistivity structure. For deeper parts, the HCZ appears slightly oblique to regional strike and located further inland than revealed by the impedance inversion models (*cf.* Figs 3d and e).

For both coordinate systems we used all four components of the impedance tensor. Final overall rms values for the two impedance inversion results are very similar, suggesting equivalent data fits for both set-ups. The overall rms error, however, is not rotationally invariant as only data variances are considered.

Closer inspection of rms distributions of impedance-only inversion results in frequency–space domain and for single data components revealed no obvious systematic misfits for either of the coordinate system set-ups. However, examination of model responses in both coordinate systems, that is, rotating the response of N00°-aligned results to N41°W and vice versa, reveals significant differences (Fig. 4). The N41°W model, which exhibits a HCZ, can explain both the *xy*- and *yx*-components of the impedance data in both coordinate systems, whereas responses of the N00° set-up do not reproduce apparent resistivities and phases of the *xy*-component when rotated to strike (blue curves in Fig. 4b). These discrepancies are related to the absence of the HCZ.

Independent line-by-line 2-D inversions along the seven profiles by Becken *et al.* (2011) revealed deep subsurface structures and a strike-aligned HCZ, similar to the results in Figs 3(b) and (e). In

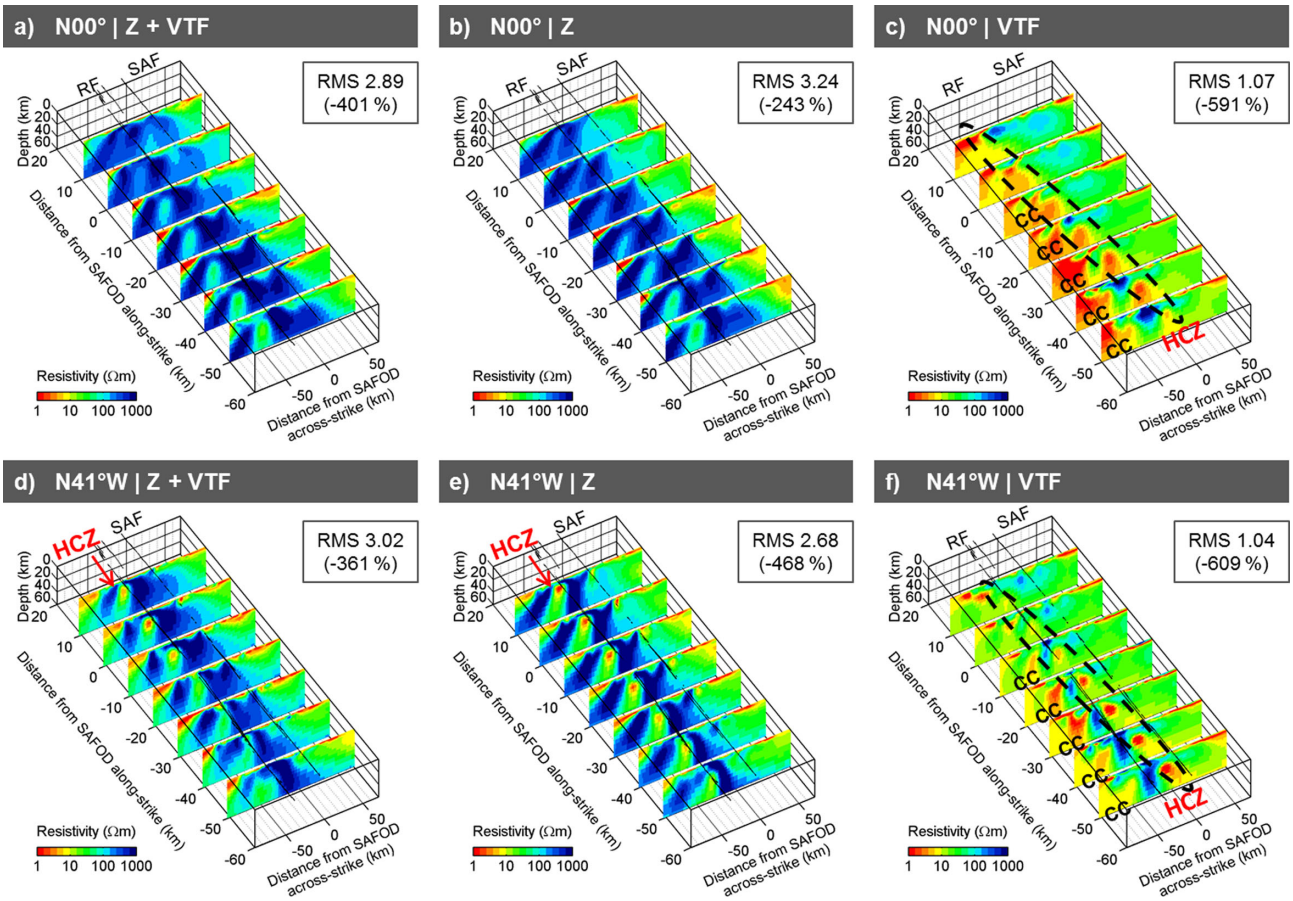

Figure 3. 3-D inversion results of the California MT array using joint and separate inversion of impedance (Z) and VTF data for two different coordinate systems; (a)–(c) geographic coordinate system (N00°), (d)–(f) strike-aligned set-up (N41°W). 3-D inversion models are displayed as slices along seven profiles (*cf.* Fig. 1). RF, Rinconada Fault. Final rms misfit and overall misfit reduction are provided in the annotations. For VTF inversion, a zone of high conductivities appears beneath the coastline (CC). *Note*. Using impedances a deep HCZ is only recovered in the strike-aligned grid.

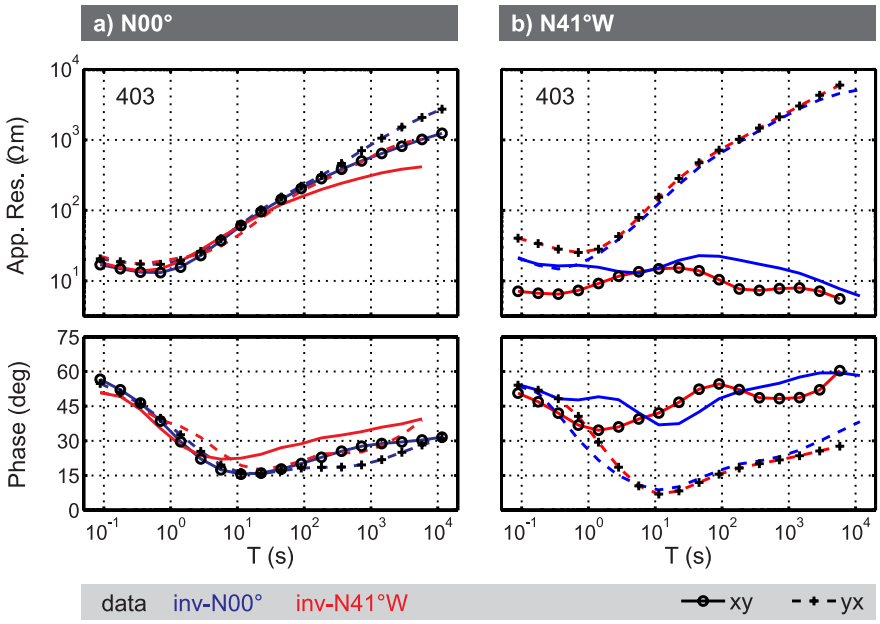

Figure 4. Comparison of observed data (symbols) and impedance-only inversion responses (dashed and solid lines) obtained in geographic (inv-N00°, *cf.* Fig. 3a) and strike-aligned (inv-N41°W, *cf.* Fig. 3c) coordinate systems. The blue lines in (a) show inversion responses of inv-N00° together with the back-rotated responses of the N41°W inversion (red lines). In (b), red lines are the results of the strike-aligned inversion and the blue lines are the inv-N00° results rotated to strike. Only the strike-aligned inversion (red curves) fits the data in both coordinate systems, while the inversion in the geographic coordinate system (blue lines) fails to fit the data in strike coordinates. The full impedance tensor was used for rotation. Site 403 is located on profile 2 (see Fig. 1).

fact, the HCZ, located between the SAF and the coast at 20–30 km depth within the high-resistive zone was essential to fit the data along profiles 2–6 with 2-D inversion.

To discuss this further, in particular resolution for structures at depth >10 km, we use complementary synthetic 3-D data sets.

4 3-D INVERSION TESTS WITH SYNTHETIC DATA

4.1 The SYNPRK model

The SYNPRK model (Fig. 5a) comprises dominant structures of the survey area near Parkfield as revealed by 2-D and some of the 3-D inversion models: A highly conductive, 20 km wide and 25 km high zone (HCZ) (1 Ωm) with its top at 17 km depth is embedded in a background structure mimicking a highly resistive Pacific Plate (2000 Ωm) and an intermediately resistive North American Plate (200 Ωm). The HCZ is located approximately 30 km southwest of the surface trace of the SAF and extends 1150 km along strike. The top layers of the model comprise sedimentary material (3 Ωm) of varying thickness (2.2–6.8 km). The Pacific Ocean (0.3 Ωm) is included according to true (3-D) bathymetry. Forward data were calculated with a station distribution similar to the field data layout (Fig. 5a) and also for a regular site layout with profile distances of 10 km and an even site spacing of 2 km along the profiles. 3 per cent Gaussian noise was added to the synthetic data. For 3-D forward modelling we used both ModEM3DMT and WinGLink (Mackie *et al.* 1994) to compare forward responses.

4.2 The inversion coordinate system and data weighting

In a first step, we examined the sensitivity of the impedance and VTF data components to the HCZ. The HCZ was removed from the SYNPRK model (SYNPRK-h, *cf.* Fig. 5b). For both coordinate systems the HCZ significantly influences both impedance and VTF data in the vicinity of the HCZ for periods >10 s, but how the effect is distributed between the various data components and their amplitudes differs between the coordinate systems. This is shown exemplarily in Fig. 6 for a (synthetic) site located on top of the HCZ. The SYNPRK model comprises predominantly 2-D structures and exhibits a clear geo-electric strike direction; the 3-D nature of the ocean and the finite along-strike extent of the HCZ constitute only weak 3-D effects. Hence, in the geographic coordinate system, the response of the strike-parallel HCZ is distributed between all components of the impedance tensor and VTFs (Fig. 6a). If data are rotated to the geo-electric strike direction, the HCZ influences predominantly the *Zxy* and *Ty* components (Fig. 6b). All other components are only marginally affected because of the low current density—and therefore low sensitivity—perpendicular to strike within the surrounding highly resistive host.

Subsequently, we tested the resolution of the HCZ in 3-D inversion. Impedances and VTFs of the SYNPRK data set (10 km × 10 km site spacing) were inverted separately using the same coordinate system, model parameters and data error settings as previously described for the California MT array data. The results in Figs 7(a)–(d) are analogous to the field data results (*cf.* Figs 3b, c, e and f). Inverting impedances (Figs 7a and b), the HCZ of the SYNPRK model is only recovered for the strike-aligned coordinate system, whereas results obtained in the geographic coordinate system suggest a homogeneous resistive deeper subsurface. In contrast, inversion of VTF data recovers the HCZ in both coordinate systems (Figs 7c and d).

The amplitudes of the impedance tensor elements are related to absolute resistivities of the subsurface: large amplitudes refer to high resistivity and small amplitudes to low resistivity. For the N00° set-up, all four impedance components of the SYNPRK data are dominated by the high resistivities of the Pacific Plate at long periods (Fig. 6a). The influence of the low-resistive HCZ appears as a minor variation in the curves. The responses of the SYNPRK-h variant are almost indistinguishable within the error bounds from the SYNPRK data. It is generally difficult for the 3-D inversion algorithm to recover the high resistivities of the Pacific Plate because

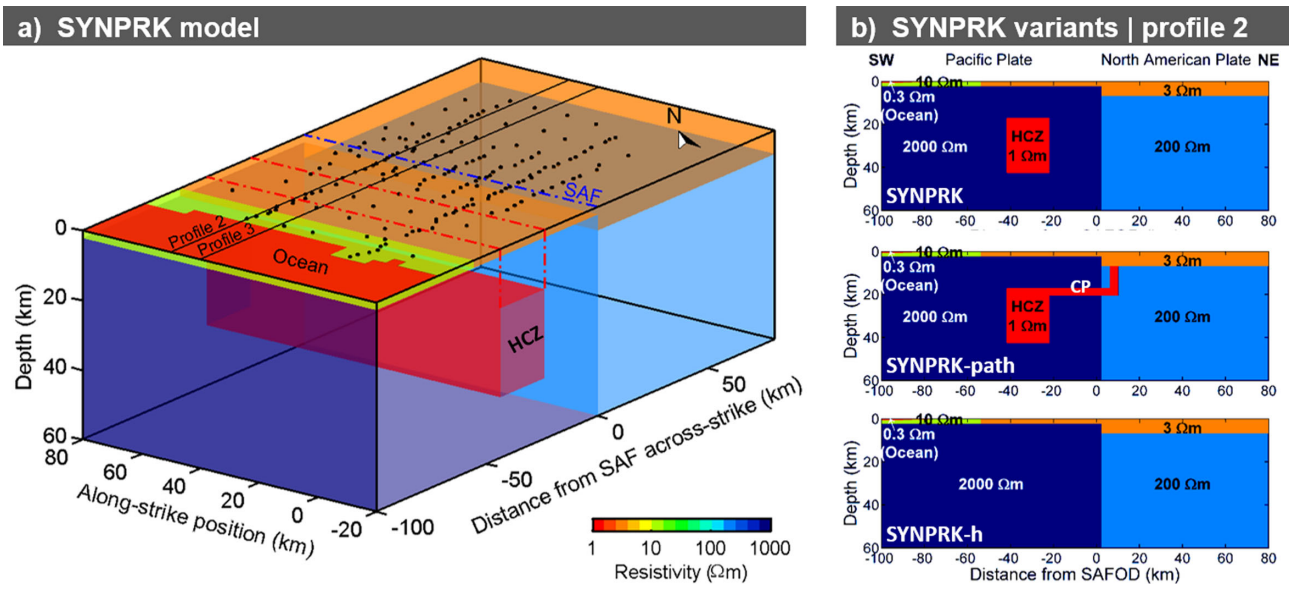

Figure 5. SYNPRK model. (a) The SYNPRK resistivity model contains the main structural features revealed by 2-D and 3-D magnetotelluric inversion. The HCZ extends 1150 km along-strike; the Pacific Ocean is integrated according to true bathymetry. All other structures extend to the model edges. (b) Modifications of the SYNPRK model include a conductive path between the deep, conductive block (HCZ) and the upper-crustal San Andreas Fault northwest of profile 3 (SYNPRK-path) and a homogeneous Pacific Plate (SYNPRK-h). These models are used to demonstrate aspects of 3-D inversion (see text).

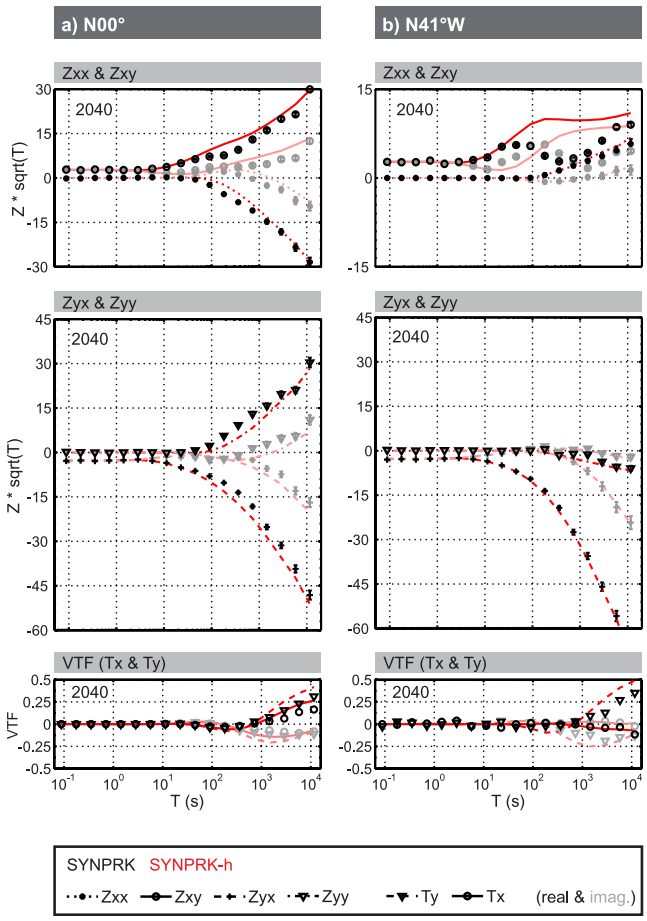

Figure 6. Responses of the SYNPRK (symbols) and the SYNPRK-h (red lines) resistivity model. See Fig. 5 for the SYNPRK model variations; site 2040 is located on profile 2 directly above the HCZ. (a) In the geographic coordinate system the responses of the SYNPRK-h model do not significantly differ from the SYNPRK data. At most periods, the *Zxx* and *Zyy* responses are indistinguishable within the error levels. (b) In a coordinate system aligned with the predominant geo-electric strike direction, the information about the HCZ concentrates in the *Zxy* component. Now, the misfit of the SYNPRK-h response and the SYNPRK data becomes significant. Note: *Zxy* has very small amplitudes and error bars are smaller than the symbol sizes.

it is necessary to overpower effects from model regularization and the low-resistive prior model (10 Ωm). In the N41°W set-up, information on the high resistivities and the HCZ are separated. The off-diagonal impedance components split up into a large component (*Zyx*) containing information about the high resistivities of the Pacific Plate and a small component (*Zxy*), in which information on the existence of a HCZ is concentrated.

VTF data do not carry information on the absolute subsurface resistivity but on relative conductivity changes. VTF amplitudes are proportional to the magnitude of lateral conductivity contrasts and vanish for homogeneous subdomains. Since we use constant errors for the VTF data and nearly homogeneous starting models, the inversion puts automatically more weight on VTF data affected by lateral conductivity contrasts (such as sites located at the edges of the HCZ) as they exhibit initially the highest misfits.

To resolve the HCZ with inversion of impedances in the N00°-aligned coordinate system, the information contained in the smaller-sized diagonal impedance elements has to be amplified by setting their error bounds to very small values (e.g. a floor <1 per cent of $|\det(Z)|^{1/2}$), Fig. 7e). In practice though, it is often not feasible to set *Zxx* and *Zyy* errors to such small values for the entire period range, because the diagonal components of field data often suffer from poor signal-to-noise ratios, particularly in noisy environments. Defining large error bounds or using (large) statistically derived error bars, however, effectively downweights or omits the information contained in the diagonal impedance elements.

In the strike-aligned coordinate system, where the information on different structures is separated, the relative weighting between the impedance components determines what is resolved. For the inversion results in Figs 7(a)–(e), we used data errors proportional to the absolute values $|Zij|$, so that each of the diagonal and off-diagonal elements is weighted the same. Various authors applying 3-D inversion to real-world data suggested to use data errors relative to the mean of the complex off-diagonal impedances $|Zxy * Zyx|^{1/2}$ (e.g. Meqbel 2009; Patro & Egbert 2011). Setting such impedance errors of 3 per cent of $|Zxy * Zyx|^{1/2}$, however, 3-D inversion of the SYNPRK data set fails to retrieve any structural details below 10 km (Fig. 7f). For the SYNPRK data such averaged errors floors effectively downweight the important but smaller *Zxy* component relative to *Zyx*.

These findings are not only important for this particular synthetic data set, but have more general implications for 3-D inversion, in particular for data sets which are dominated by regional 2-D structures. The full impedance and VTF data contain all information independent of the coordinate system and no information is lost by rotating the impedance tensor. However, as only data variances are considered by the 3-D inversion, that is, dependencies between data components are neglected, data weighting is influenced by the chosen coordinate system. In 3-D situations with a pronounced regional 2-D structure, dependencies between individual data components are minimal in a strike-aligned coordinate system. Effectively, the off-diagonal elements decouple into TE- and TM-mode equivalents and therefore, rotation to strike results in a suitable data weighting. To further examine 3-D inversion of the SYNPRK data set, we concentrate on the strike-aligned coordinate system.

4.3 Prior model and smoothing

A second important factor influencing recovery of subsurface structures is the resistivity distribution of the *a priori* model. To investigate this we used the off-diagonal impedances only (error bounds 3 per cent of $|Zij|$). Using prior model resistivities >10 Ωm, the HCZ of the SYNPRK structure is less clearly expressed (20 Ωm, Fig. 7g) and disappears completely for values of 50 Ωm and above. Nevertheless, final rms values are similar and acceptable and do not reflect these strong differences and – with respect to the deep HCZ – inadequate inversion results. This mystery is solved when misfit values are assessed in more detail (Fig. 8). For a background resistivity of 20 Ωm the missing HCZ leads to elevated *Zxy* misfits at sites located above the conductor (Fig. 8b). In contrast, the fit of the *Zyx* component is improved compared to the 10 Ωm (Fig. 8a) result because higher prior model resistivities allow easier realization of the stark resistivity contrast between the Pacific Plate (2000 Ωm) and the ocean (0.3 Ωm). Hence, the impedance component, which is on average closer to the resistivity level of the prior model is better fit by the inversion.

If smoothing is disabled across the edges of the HCZ, the inversion does recover the HCZ even when using a homogeneous 50 Ωm background *a priori* (Fig. 7h). This approach represents

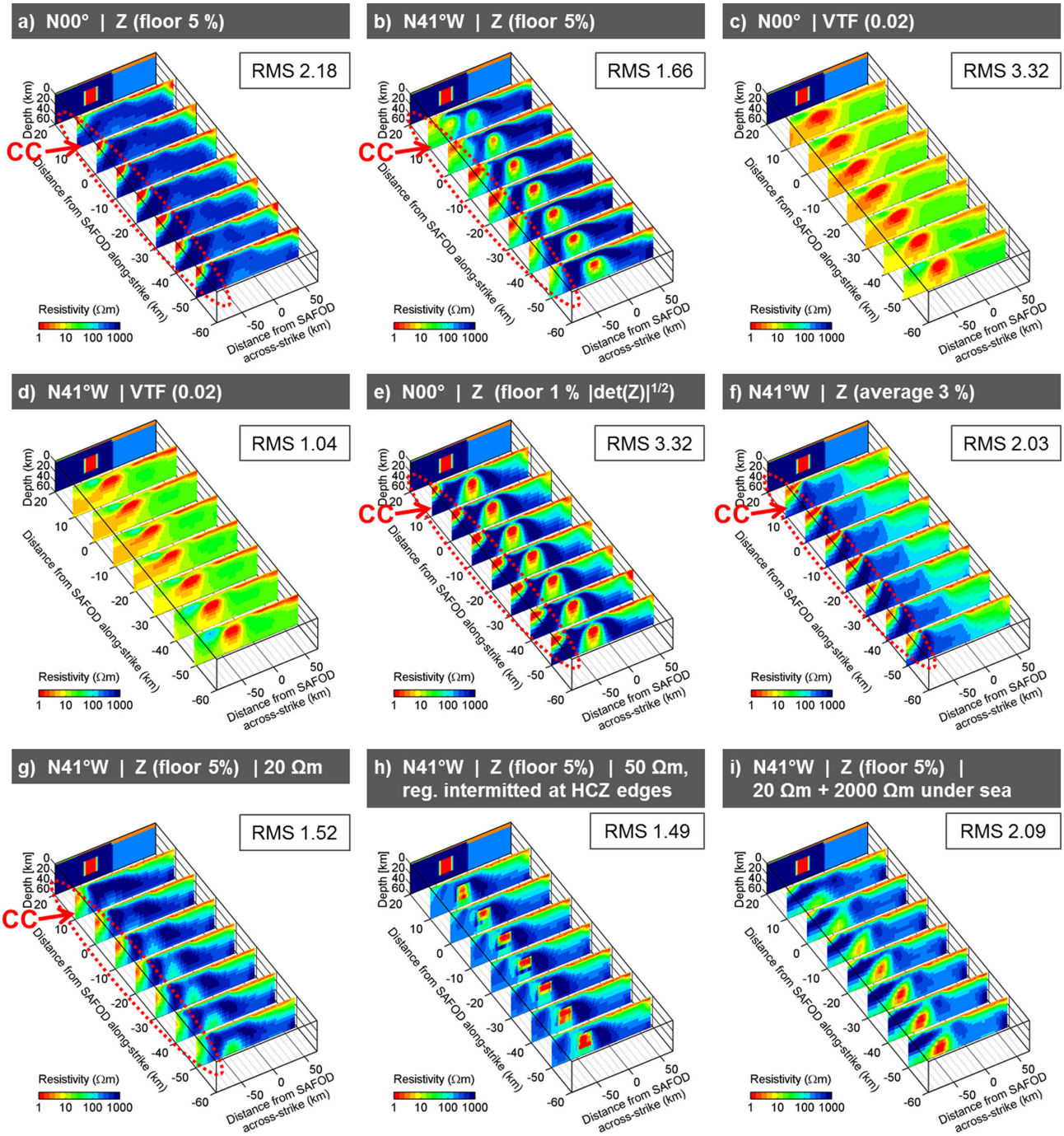

Figure 7. 3-D inversion of synthetic data (SYNRPK model) using different data weighting and prior models. The background slice at $x = 20$ km shows a slice through the SYNPRK model for comparison. (a) and (b) 3-D inversion of the synthetic SYNPRK impedance data (errors 3 per cent of $|Zij|$, diagonal elements floor 5 per cent of $|Zxy * Zyx|^{1/2}$) recovers the deep HCZ only in the strike-aligned coordinate system. (c) and (d) Using only VTF data 3-D inversion reveals a HCZ independently of the orientation of the inversion coordinate system. (e) Imaging the HCZ in the geographic coordinate system succeeds only if extremely narrow error bounds are applied to diagonal impedance elements (e.g. 1 per cent of $|\det(Z)|^{1/2}$). (f) Averaging impedance error floors in the strike-aligned set-up downweights the smaller Zxy component and a HCZ is not revealed. (g) The HCZ disappears if initial background resistivities are set too high (>20 Ωm). (h) With intermitted regularization across the edges of the HCZ, the inversion recovers the HCZ even for high starting resistivities. (i) Inclusion of high resistivities beneath the ocean (outside the displayed area) *a priori*, results in a continuous resistive Pacific Plate across the coastline and facilitates the recovery of the HCZ. Please note, the inversion introduces artificial conductive zones (CC) along the coastline for some of the inversion results (a, b, e–g).

only a weak constraint, as the inversion is still allowed to produce a smooth conductivity structure across the domain boundaries. Applying a lower regularization in both horizontal directions, however, leads to a generally feebler expression of the deep structures, but does not improve the recovery of the HCZ itself. Obviously, the chosen prior model and smoothness constraints operate interrelated and in combination influence the outcome of the inversion.

Several inversion models reveal cells with high conductivity beneath the coastline (labelled CC in Figs 7a, b, e–g). This effect disappears if a 2000 Ωm half-layer is included *a priori* beneath

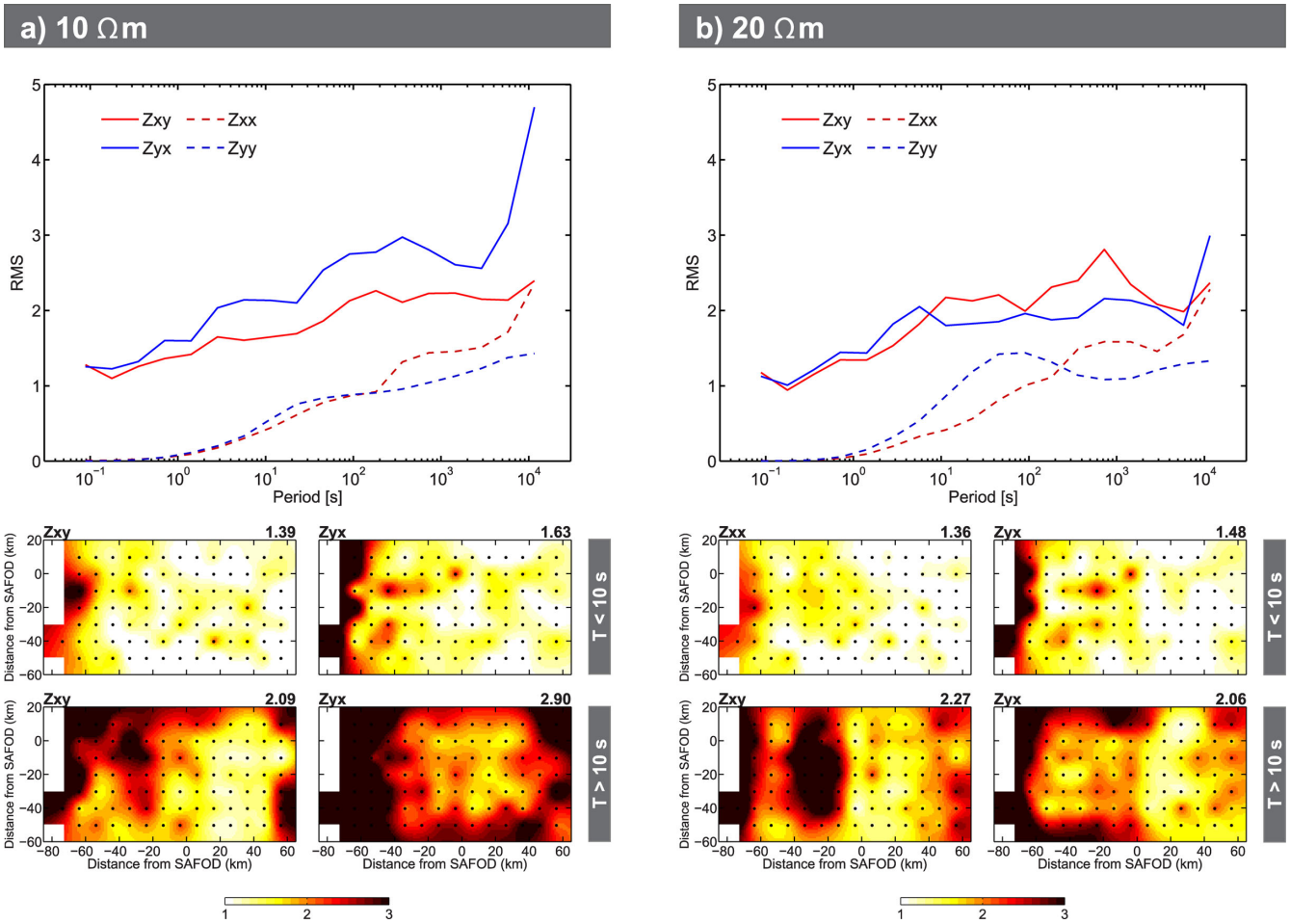

Figure 8. Distribution of rms errors in frequency–space domain of final inversion results of the SYNPRK data set using starting/prior model resistivities of 10 Ωm (a) (*cf.* Fig. 7b) and 20 Ωm (b) (*cf.* Fig. 7g). Upper panel shows rms errors for each of the four impedance component versus period at all sites, the lower panels show rms errors for *Zxy* and *Zyx* at each site for periods below and above 10 s.

the ocean from −120 km across-strike distance from SAFOD towards the southwestern model edge (i.e. outside the displayed area). Then, 3-D inversion recovers a continuous high-resistive Pacific Plate across the coastline (Fig. 7i) and the HCZ, which is bound to the smaller *Zxy* component. With the inclusion of conductor CC (Figs 7a–g), the 3-D inversion attempts to add a resistivity contrast between the conductive ocean and the high-resistive Pacific Plate. While we know that CC is a spurious feature, it fits the data and such a solution is closer to the prior model. For the inversion, this result is less costly in terms of a desired minimal model norm than the true SYNPRK structure. We would like to point out that such artefacts are not a particularity of the ModEM inversion scheme or 3-D inversion *per se* but a general problem for any overparametrized inversion.

Moreover, the results of Figs 7(h) and (i) show that providing *a priori* information can significantly alter and improve the outcome of 3-D MT inversion. They also illustrate that it is important to match the resistivity structure outside of the inner model domain as accurately as possible. More detailed investigation of such approaches should be addressed in the future to better understand 3-D MT inversion and allow an integrated interpretation of MT measurements and other geophysical data. A review of Bedrosian (2007) based on 2-D modelling and inversion compares a range of approaches for integration of *a priori* information and illustrates their value in revealing the underground structure.

5 3-D INVERSION OF THE CALIFORNIA DATA SET

5.1 3-D inversion results

Following the resolution tests with the synthetic data, all subsequent 3-D inversions were performed in the strike-aligned coordinate system, in which TE and TM modes are mostly decoupled. To illustrate the contribution of each of the 'modes' to the outcome of the inversion, we inverted both off-diagonal impedances components (*Zxy*, *Zyx*) of the 73-site data set separately (error bounds 3 per cent of $|Zij|$). This approach is similar to a 2-D TE- or TM-mode-only inversion. Consequently, the 3-D inversion results in Figs 9(a) and (b) show two complementary pictures of the geo-electric subsurface structures. When inverting only the *Zxy* component (Fig. 9a), we obtain as a main feature a HCZ at depth extending parallel to the SAF. The shape of the HCZ and its top varies along-strike and the HCZ is connected to surface with a conductive channel beneath profiles 2 and 3. Inversion of *Zyx* in Fig. 9(b), on the other hand, yields high resistivities (500–3000 Ωm), which are far off the 10 Ωm conductive prior model. Using both off-diagonal impedances and the same error bounds, 3-D inversion is dominated by the regional scale, mostly 2-D subsurface structures (Fig. 9c). Smaller 3-D features, such as a subvertical conductive zone, which appeared close to the SAF when inverting all four impedance components (*cf.* Fig. 3e),

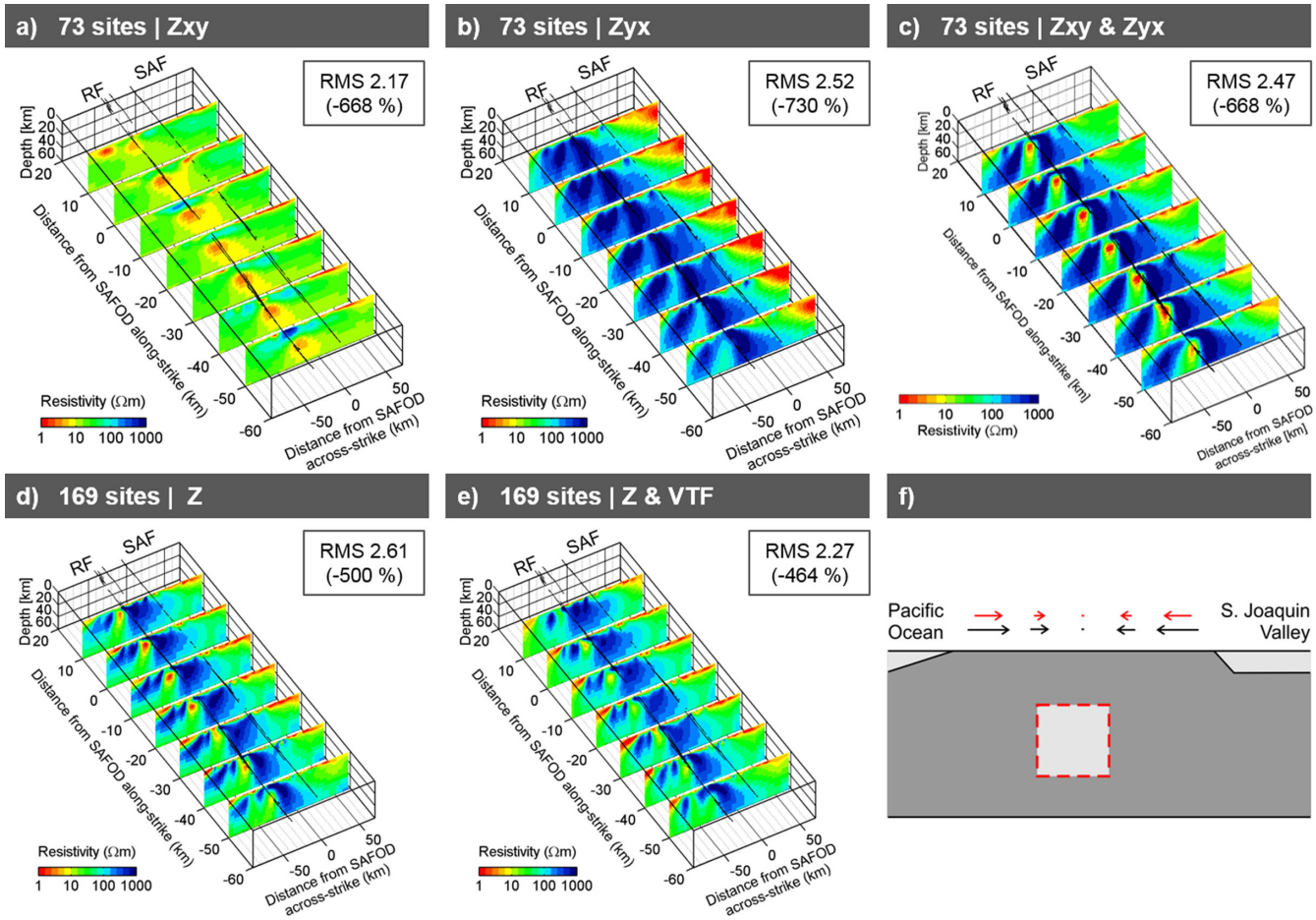

Figure 9. 3-D inversion results of the data from California for two site layouts (*cf.* Fig. 1) and different data set-ups. (a) and (b) Separate 3-D inversion of both off-diagonal impedances show two complementary pictures of the subsurface. Whereas (a) *Zxy* inversion recovers the HCZ, results for (b) *Zyx* yield extended zones of high resistivities at depth to accommodate for the strong split of impedance tensor components in TE and TM mode. (c) If only off-diagonal impedances are used 3-D inversion recovers the 2-D regional resistivity structure, 3-D along-strike variations of the conductivity structure, that is, the subvertical conductive zones (CP?) close to the SAF beneath profiles 2 and 3 are not resolved (d) and (e) 169 sites. (f) Ocean and sediments of the San Joaquin valley dominate VTF behaviour across strike (*Ty*). Induction vectors are in the Wiese convention. A conductor (dashed red outline) at depth between Pacific Ocean and San Joaquin valley causes oppositely directed and induction vector amplitudes which lead to more rapidly decreasing total induction vectors (red arrows). Equivalent induction vector behaviour can be achieved with overall lower resistivity between the ocean and the San Joaquin valley (*cf.* (e)).

however, are not recovered as information of the diagonal elements was not included.

Finally, we included more sites from the densely sampled areas. We used 169 sites in total (*cf.* Fig. 1) and discretization of the subsurface was refined to 2 km × 2 km for the central part of the mesh (40 × 80 × 57), which increases the total number of model parameters to 70 × 110 × 57. The sizes of the horizontal padding planes were recalculated, using a lateral increase factor of 1.3. As before, we applied higher model smoothness constraints along-strike.

Now, site density is higher in the central parts of the array close to the SAF but decreases towards the edges. Additional tests with the SYNPRK data showed for the 169-site layout a decrease in resolution for the high resistivities at depth towards the coast and further beneath the Pacific Ocean. 3-D modelling studies of Mackie *et al.* (1996) indicated high sensitivity of land data in California to the resistivity structure of the oceanic crust and mantle. Therefore, we added a 1000 Ωm half-layer (thickness: 60 km) *a priori* beneath the ocean extending from $y = -120$ km to the southeastern model boundary for inversion of the field data (see also Section 4.3). All other inversion parameters, including error bounds for impedances and VTFs were kept the same (*cf.* Fig. 3). 3-D inversion results for impedance-only and joint impedance + VTF inversion are shown in Figs 9(d) and (e), respectively.

With 169 sites, the regional scale structure is modelled very similarly to previous results obtained with the 73-site data set (*cf.* Fig. 3). The conductivity of the HCZ, however, shows more variation along-strike. Higher conductivity is found beneath the northwestern profiles, which decreases towards the southeast. In addition, the HCZ appears slightly narrower than for the 73 sites subset (*cf.* Figs 3d–e), especially if VTFs are included (Fig. 9e). Impedance misfits for the joint inversion model (Fig. 9e) are slightly higher for sites on top of the HCZ. Rather unexpectedly, the HCZ appears less pronounced with joint impedance + VTF inversion. VTFs are sensitive to lateral conductivity contrasts but 3-D forward modelling tests revealed that the highly conductive sedimentary cover has a strong shielding effect. The HCZ influences the VTFs only at periods >50 s. In the survey area, saline water of the Pacific Ocean and thick, low-resistive sediments of the San Joaquin valley are two large-scale, predominantly 2-D regional conductors, in contrast to the much higher-resistive subsurface (Fig. 9f). Lateral conductivity contrasts have a far-reaching effect on the profile-parallel VTF component (*Ty*) at intermediate to long periods. This can be best

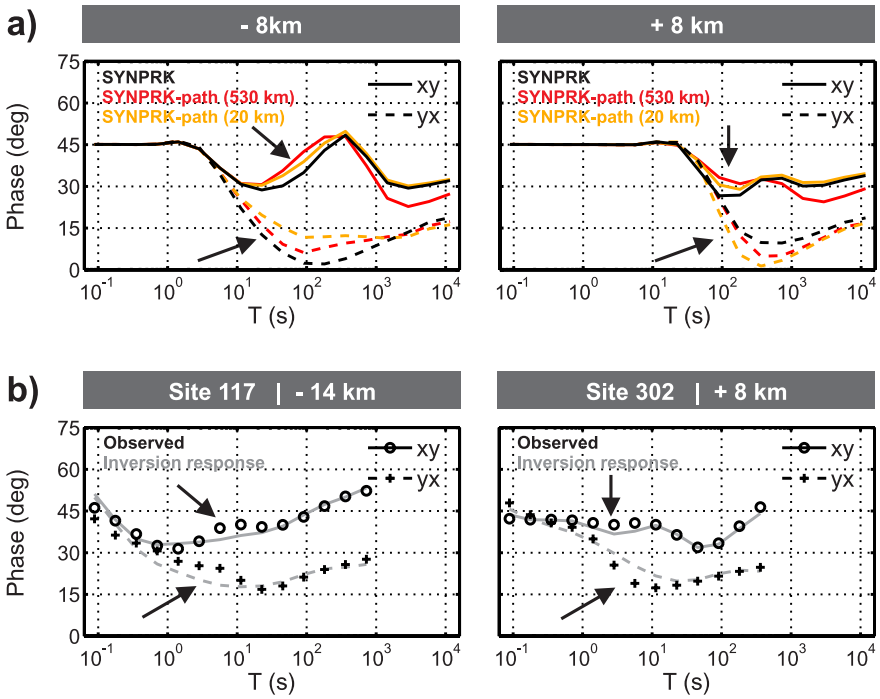

Figure 10. CP between HCZ and SAF: (a) Comparison of SYNPRK-path and SYNPRK phase responses along profile 2 at ±8 km distance from where the CP reaches surface. The influence of the CP is expressed in systematic phase changes from the SYNPRK response on either side of the CP outcrop (indicated by arrows). (b) For the field data, systematic phase misfit patterns can be found between observed data and inversion model responses at sites located along profile 2 on both sides of the point where the CP reaches surface in the 2-D results. The deviation pattern is similar to the differences between SYNPRK and SYNPRK-path data (arrows, *cf.* (a)). This behaviour suggests that the misfit for the field data is related to the absence of the CP in the inversion results.

demonstrated if VTFs are presented as induction vectors. In the Wiese convention, the induction vectors tend to point away from conductors. Induction vector amplitudes decrease with increasing distance from the boundaries and both effects cancel out in the middle. The *Ty* contribution of the HCZ (dashed red line in Fig. 9f) is relatively small and oppositely directed. Effectively this leads to induction vector amplitudes decreasing more rapidly when moving away from the conductivity contrasts (red arrows in Fig. 9f). In this simplified case, the same induction vector behaviour can be produced if the (isolated) HCZ is replaced with an overall lower resistivity between the coast and the San Joaquin valley. The inversion result in Fig. 9(e) suggests that model regularization (smoothing) is in this case suppressing a more focused appearance of the HCZ.

5.2 A conductive path (CP) into the seismogenic SAF system

As stated before, the 3-D subsurface images are generally in good agreement with the 2-D inversion results (*cf.* fig. 1(b) in Becken *et al.* 2011). A prominent difference is the absence of a CP between the HCZ at depth and the SAF beneath profiles 2 and 3 in the 3-D inversion models. The CP appeared, however, for the *xy*-impedance-only inversion (*cf.* Fig. 9a). Two possible explanations for the absence of the CP come to mind: (i) the CP is an artefact introduced by limitations of 2-D inversion or (ii) 3-D inversion cannot resolve this structural detail.

This will be investigated further with 3-D inversion of synthetic data. The SYNPRK-path model includes a CP northwest of profile 3 (Fig. 5b). Fig. 10(a) compares responses of the SYNPRK model and the SYNPRK-path variants for 20 and 530 km along-strike extent of the CP. The deviation pattern between SYNPRK-path and SYNPRK responses is similar to the differences between observed and modelled field data (arrows in Figs 10a and b). This suggests that a CP linking the HCZ with surface could exists but this feature is not recovered by 3-D inversion given the specified error bounds and chosen regularization.

For the SYNPRK-path data sets, 3-D inversion does not recover the CP for inversion of impedances (error bounds 3 per cent, Fig. 11a) even when including VTFs (Fig. 11b). A hint to the CP in the 3-D result is the vertical conductor where the CP reaches surface (upper panels 10a and b) and a slightly reduced background resistivity beneath the SAF for the northern profiles. In contrast, *xy*-impedance-only inversion reveals a connection to the deep conductive body (Fig. 11c) similar to the results for the measured data (*cf.* Fig. 10a). Downweighting the *Zyx* and *Zyy* components (Fig. 11d) reduces the influence of the ocean effect on the inversion result and 3-D inversion recovers a clear image of the CP for the 530-km-long variant, but not if the along-strike extent is only 20 km. 2-D inversion of the SYNPRK-path data set along profile 2, using the same site configuration, immediately recovers the CP for both 20 and 530 km along-strike extent using standard inversion settings and error floors (Fig. 11e). Using a denser site spacing for the 3-D inversion does not improve the recovery of the CP. A CP is only recovered, though if all four impedance tensor components are used. At least none of our trials with off-diagonal impedance elements-only inversions produced the CP.

For the 3-D results in Figs 10(a) and (b), where the CP is not recovered, data misfits are dominated by poor reproduction of the coastal resistivity contrast, which was already described for the SYNPRK model (*cf.* Fig. 7). However, visual inspection of apparent resistivity and phase curves reveals misfits at sites near the SAF similar to those described for the field data inversion results (*cf.* Fig. 10b). For all these inversion results, a pronounced conductor

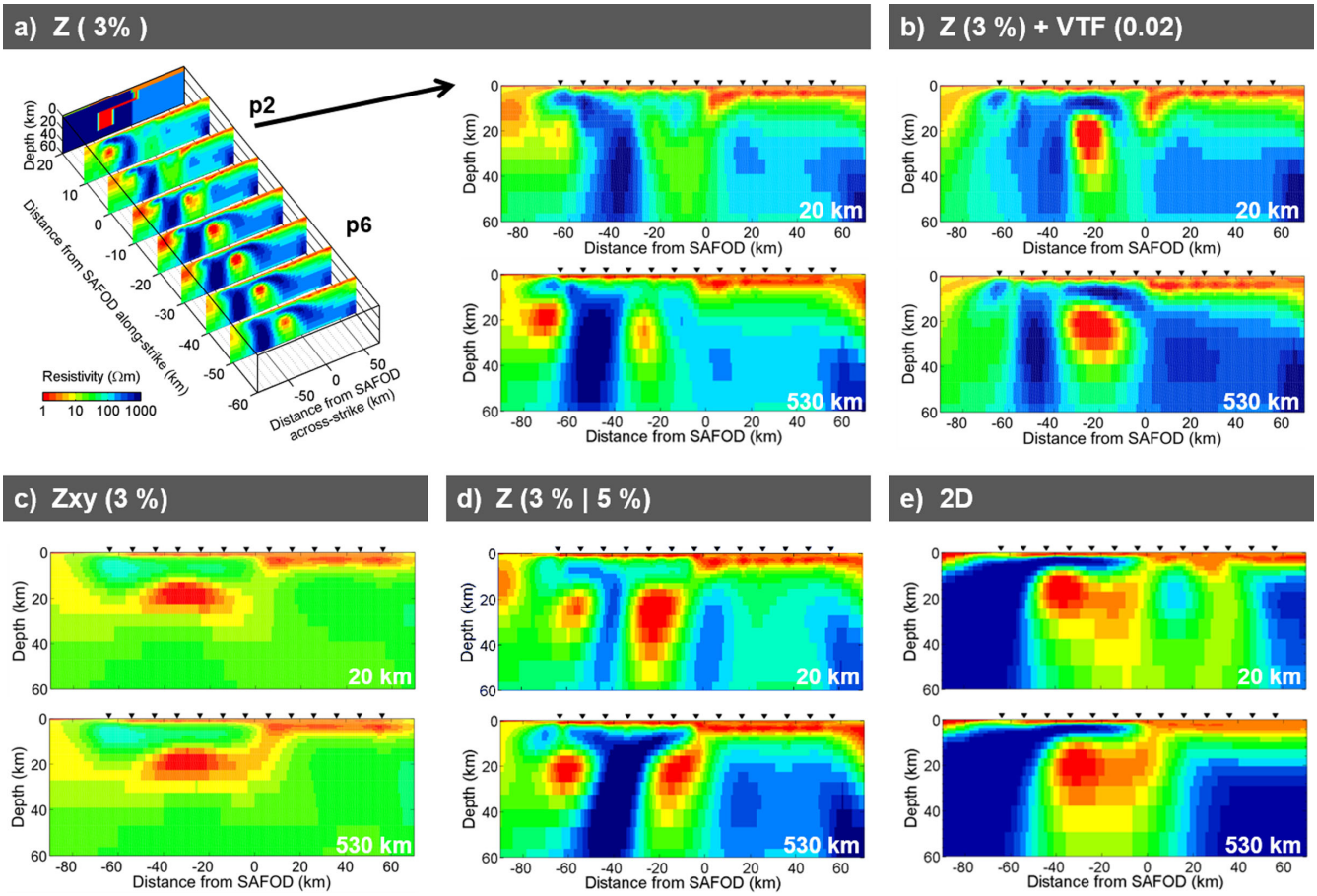

Figure 11. 3-D and 2-D inversion results of SYNPRK-path (*cf.* Fig. 5b) data sets for 20 km (upper panels) and 530 km (lower panels) along-strike extent of the CP. Four-component impedance (a) or joint impedance + VTF (b) inversion using same error floors as for the California data set reveal an isolated HCZ; (c) *Zxy*-only inversion, on the other hand, does recover the CP. (d) In 3-D inversion of the full impedance tensor, the CP can only be recovered if error bounds for *Zxx* and *Zxy* (3 per cent) are smaller than for *Zyx* and *Zyy* (5 per cent). (e) 2-D inversion immediately recovers the CP for both 20 and 530 km along-strike extent.

(CC) appears in the coastal area. Such a spurious structure was also observed for the SYNPRK inversion model (*cf.* Figs 7a, b, e–g). Conductor CC is more clearly expressed in the SYNPRK-path results and inclusion of VTFs does not suppress this structure. Replacing the CC with higher resistivities, we find the diagonal impedances most severely affected as their amplitudes are reduced at long periods. This suggests a conductivity contrast in the coastal area provides an alternative way for the inversion to explain the SYNPRK-path data, at least the *xx*-impedances and partly the *yy*-impedances.

In summary, 3-D inversion can only recover a CP if it is (i) elongated along-strike for at least 150 km and (ii) the impedance components affected by the ocean effect (mainly *Zyx*) are down-weighted. In all other cases, only hints of its existence are revealed. In practice, however, such weak indications would only be recognized and interpreted correctly if the true underlying structure was known beforehand. Examining the data fit for the synthetic data site by site, the misfit caused by the absence of the CP is minor compared to the general data fit quality. Hence, no pronounced systematic misfit is observed for the models without a CP. Please keep in mind that all of the above findings are for 3-D inversion of (perfect) 3-D synthetic data.

For the California data set, it is therefore probably not possible to resolve the CP with 3-D inversion. The most explicit hint to its possible existence is given in two of the 73-site inversion results (Figs 9e and 3e), where a subvertical conductor appears close to the SAF beneath profiles 2 and 3, at the location where the CP reaches surface in the 2-D inversion results. Manual inclusion of a CP in the final 3-D inversion models shows a significant effect on the phases of the *xy* and *yx* components between 5 and 100 s. The phase effect is similar to our observations at sites 117 and 301 in Fig. 10 but at shorter periods. In summary, a CP is consistent with the data but not a requirement to fit the data.

5.3 Preferred 3-D inversion model

Comparing the 3-D inversion results of the California data set and considering the results of the SYNPRK and SYNPRK-path model studies, we chose the inversion result of Fig. 9(d) as our preferred model (PRK-3D). The inversion is based on impedances from 169 sites and includes *a priori* high resistivities beneath the Pacific Ocean; the VTF data are not used. Fig. 12 shows the PRK-3D inversion result at four horizontal depth slices.

The upper 250 m of the model exhibit a highly variable, small-scale resistivity pattern (Fig. 12a), which is how 3-D inversion compensates for (small amounts of) galvanic distortion. The surficial features appear stretched along the SAF-parallel axis as a higher smoothing was enforced in this direction. At mid-range depths (<10 km, Figs 12b and c), the 3-D resistivity structure is

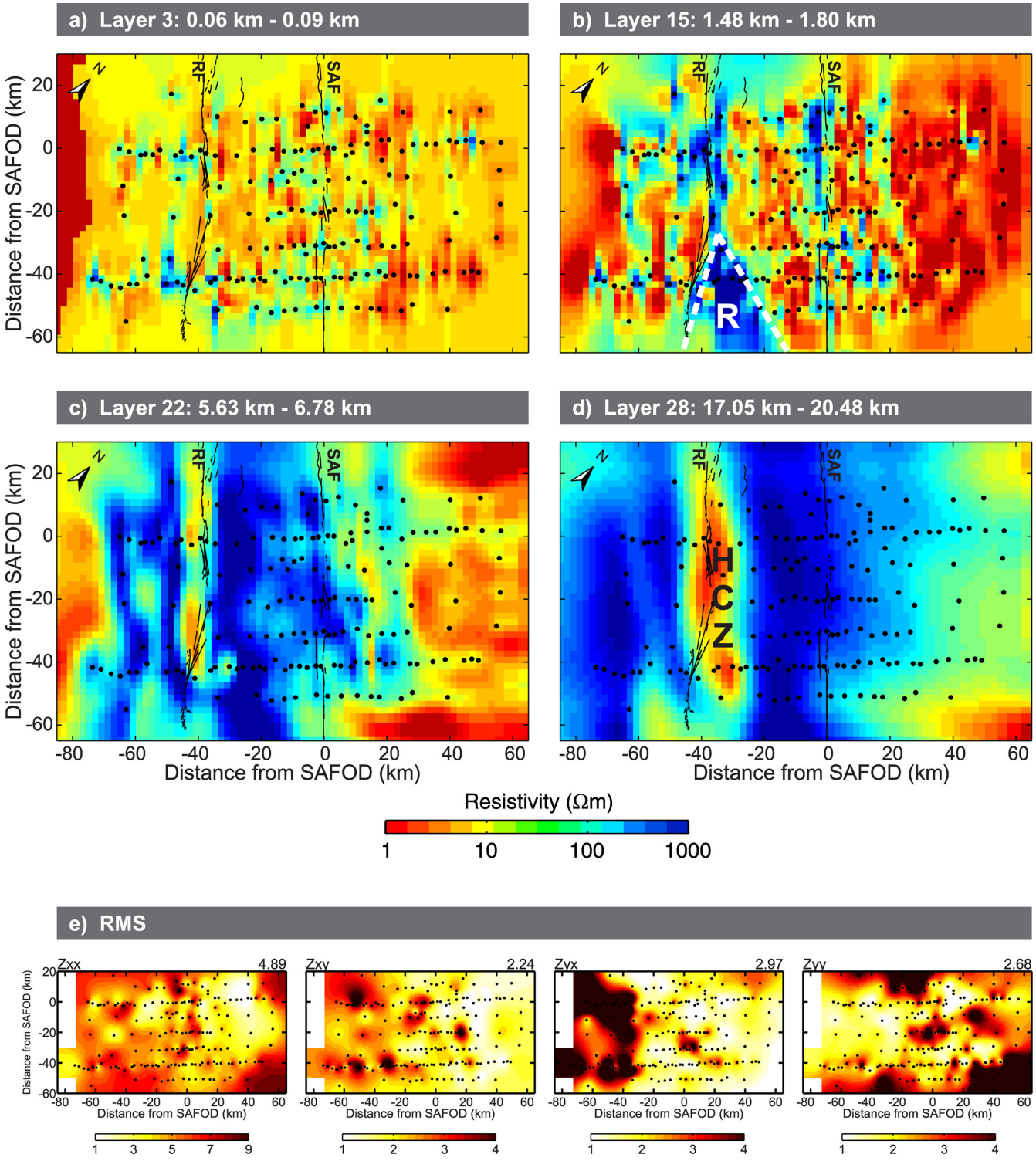

Figure 12. (a)–(d) Horizontal slices of the preferred 3-D inversion model (PRK-3D, *cf.* Fig. 9d) at various depths. (a) Variable, small-scale structures in the top layers illustrates how 3-D inversion accounts for static shift in the model. (b) and (c) The thickness of the low-resistive sedimentary cover varies between 2 km on the Pacific side of the SAF and 9 km at the northwestern profile ends. The resistive wedge (*R*) at 1–4 km depth in the southwestern survey area is important to fit VTF data in this area. (d) At depths >10 km, a zone of HCZ extends parallel to the regional strike direction. (e) Misfit distributions for the PRK-3D response show a uniform data fit. However, data misfits, in particular *Zyx* misfits, increase towards the coast.

dominated by a conductive (0.1–5 Ωm) sequence with a thickness of approximately 2 km in most parts of the array, which reaches 5–9 km in the San Joaquin valley. In areas close to the coast and along the surface traces of the San Andreas and Rinconada faults the conductive layer thins out and zones of high resistivities (1000 Ωm) reach close to surface. At mid-crustal levels (approximately 10–20 km, Fig. 12d), the model reveals resistive structures (200–2000 Ωm) extending from the coast to the SAF. A 10–20 km wide region west of the SAF appears as conductive (1–10 Ωm); this zone (HCZ) extends parallel to the SAF with its top located between 9 and 17 km depth.

Throughout the array, the data fit is of similarly good quality, yielding an overall rms of 2.61. Investigation of the misfit values in the frequency–space domain revealed smooth and homogeneous distribution for all components (Fig. 12e). However, we still observe moderate increase of misfit values towards the ocean and long periods for impedance components *Zyx* and *Zxx*, which are sensitive to the high resistivities of the Pacific Plate (*cf.* Fig. 6b).

6 COMPARISON OF 3-D AND 2-D INVERSION RESULTS

3-D and 2-D inversion results of the measured data are displayed in Figs 3, 9 and 12; direct comparisons of selected profile traces can be found in Fig. 13; data fits at selected sites are provided in Fig. 14. The 2-D results were obtained with the code of Rodi & Mackie (2001).

For the upper 10 km, 3-D and 2-D inversion result in very similar resistivity structures. Along the seven profile traces, the lateral variations of the conductive sedimentary cover agree remarkably well, although larger site distances and a much coarser subsurface discretization were used for 3-D modelling (Fig. 13). Structural differences in this depth range are small-scale, occurring for some isolated (3-D) resistivity features (A; Fig. 13a) or where measurements are severely affected by galvanic distortion (site 408 in Fig. 13a).

At depths below 10 km, the subsurface images of 3-D and 2-D models are in principle consistent (Figs 9d and 13). They reveal a SAF-parallel HCZ embedded in a high-resistive background and the absolute resistivity levels are very similar. The HCZ appears consistently with its southwestern edge located at about 40 km west of the SAF beneath profiles 1–6 (Fig. 9d). For 2-D inversion, the depth to the top of the HCZ is a very robust and well-defined feature with a slight dip towards SE (15–20 km, Becken *et al.* 2011). In 3-D inversion, this zone appears at slightly shallower depth (9–17 km, NW–SE) and surficial structures are often more conductive (Fig. 13a).

In the 3-D inversions the HCZ exhibits a similar across-strike extent of 10–15 km beneath all profiles at approximately 15–20 km depth (Fig. 12d). 2-D inversion reveals this zone as wider (20–35 km; profiles 1–5, 7) and more variable in both horizontal and depth extent. This is consistent with the synthetic studies for which we observed similarly narrower low-resistive zones for the SYN-PRK and SYPRK-path data when compared to 2-D results (*cf.* Fig. 11). For 3-D, along-strike variability is suppressed, as a relatively strong smoothing is applied. Applying a lower regularization parallel to the SAF, however, leads to a generally feebler expression of the deep structures, but not more pronounced along-strike variations.

Differences in the deep resistivity structure of 3-D and 2-D results are revealed for profile 2 (Fig. 13a). Here, the cross-sectional area of the HCZ differs significantly. The CP, which links the HCZ with the seismogenic SAF in the 2-D results, does not appear in 3-D (*cf.* Fig. 11). The absence of the CP in the 3-D results causes small, but systematic deviations of the *yx*-impedance phases for periods of 1–10 s (Fig. 14b, *cf.* Fig. 10) in this area. Modelling studies indicated that even with synthetic data a CP is not resolved by 3-D inversion (*cf.* Fig. 11).

For profile 6, images of shallow and deep resistivity structures are very similar for the 3-D and 2-D inversion models (Fig. 13b); width and conductance of the HCZ are slightly higher in 3-D. For once the HCZ is imaged shallower in 2-D than in 3-D and shallower than in the 2-D models for the other six profiles (see Becken

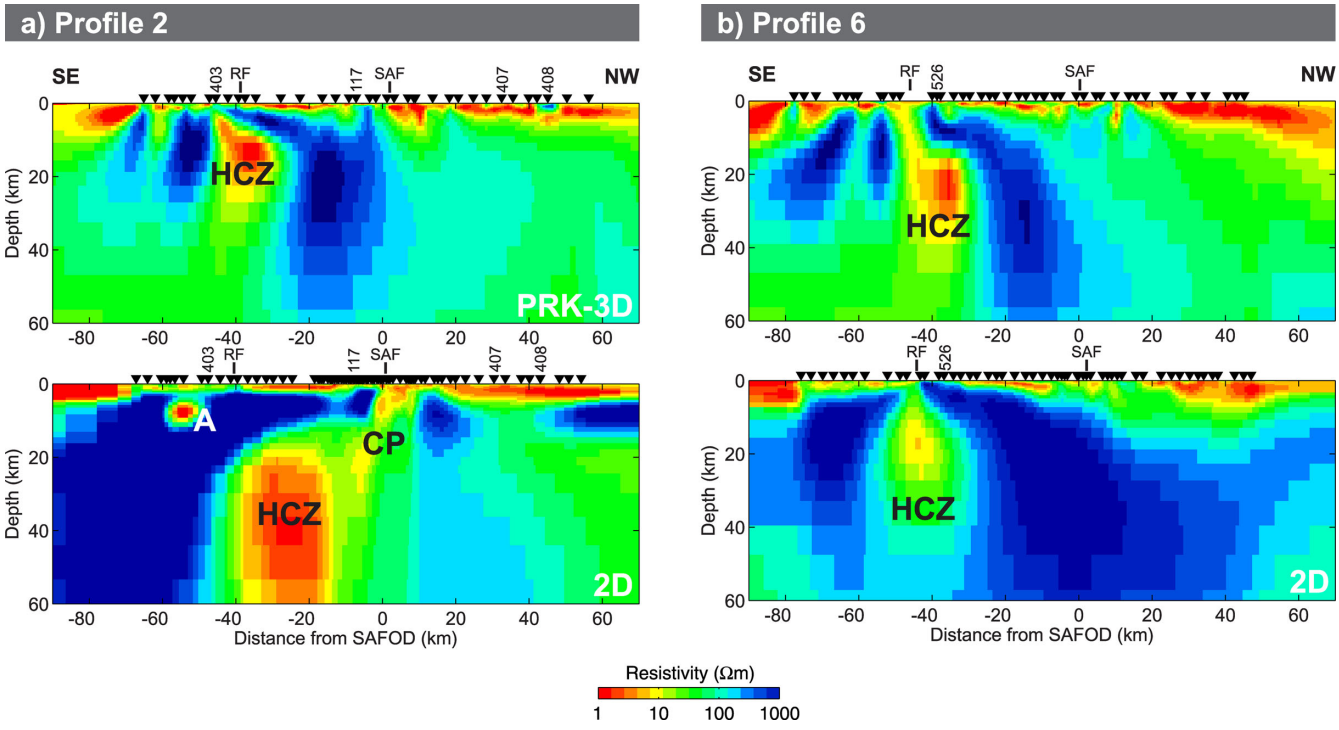

Figure 13. Comparison of PRK-3D (*cf.* Fig. 9(d)) and 2D results (Becken *et al.* 2011) along profiles 2 and 6. 3-D and 2-D inversion results are in general consistent, in particular, for the upper 10 km where differences are only small scale, for example, feature A beneath profile 2. (a) The HCZ is systematically narrower in 3-D inversion results, which is most pronounced beneath profile 2. Moreover, the CP connecting the HCZ to the SAF does not appear in 3-D inversion. (b) Along profile 6, 3-D and 2-D results are very similar for the entire depth range. 3-D responses, however, explain the data in this area significantly better than the 2-D result as the 3-D model includes significant off-profile structures in the upper 4 km (*cf.* Fig. 12b).

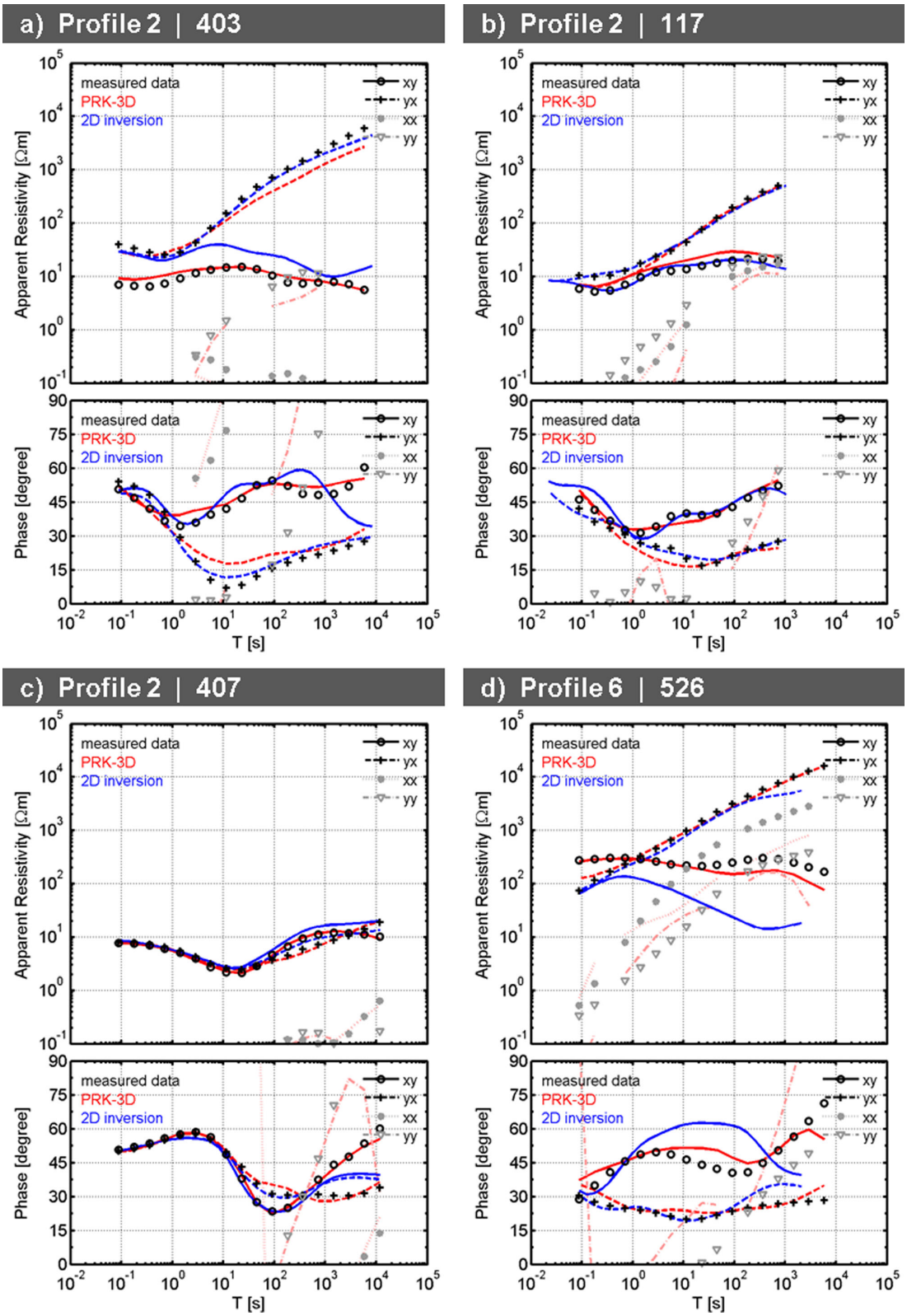

Figure 14. Comparison of PRK-3D and 2-D responses at sites along profiles 2(a)–(c) and 6(d). Site locations are marked in Fig. 13.

et al. 2011, supplementary). Becken *et al.* (2011, supplementary) indicate that the inverted quantities of this profile section were not entirely consistent with 2-D assumptions and, hence, geometry of the HCZ in the 2-D results could be influenced by 3-D effects in the data. In this region, 3-D inversion reveals a highly resistive wedge (labelled *R* in Fig. 12b) at 1–4 km depth beneath the surface trace of the Rinconada Fault, which widens towards the southeast. Forward modelling tests show, that this resistive structure is very important to fit the impedances and VTFs, which have a strong off-profile component in this area. Consequently, 3-D inversion can

explain the measured data along profile 6 significantly better than 2-D inversion (Fig. 14d).

In 2-D modelling, the HCZ extends 'infinitely' along-strike. In the 3-D models the HCZ is continued beyond the southeastern edge of the station array at depths >20 km, whereas it stops at the northwestern edge (Fig. 12d). Forward modelling tests based on the PRK-3D model suggest a minimum HCZ extension of 40 km beyond profile 7. It is not possible to define a length for the northwestward continuation of the HCZ but the overall minimum along-strike extent of the HCZ measures approximately 100 km.

7 DISCUSSION AND CONCLUSIONS

3-D MT inversion was systematically tested with a large real-world and complementary synthetic data sets. The inversion results were robust with respect to existence, size and position of regional-scale conductivity structures. At the same time, unexpected obstacles and pitfalls were revealed.

The outcome of 3-D inversion is not always independent of the coordinate system, even if the full impedance tensor is used. In general 3-D situations, impedance tensor components are interrelated. In inversion with ModEM or other 3-D inversion codes, however, impedance components are handled independently as data covariances are not taken into account. In practice the best approach is to work in a coordinate system where the coupling of different components is minimized and current systems have strongest separation, that is, aligned with the predominant geo-electric strike direction. For both, the California and the SYNPRK, data sets the extended HCZs at depth could only be reliably recovered if data and model grid were rotated to the dominant strike direction of the SAF system. Detailed strike analysis of the data set is therefore an essential pre-processing step for 3-D inversion. If a dominant strike direction can be identified, alignment of the inversion coordinate system with strike is strongly recommended.

Further important controls for 3-D inversion are sensible data-weighting schemes, taking relative sizes of components into account. Where amplitudes of individual impedance components significantly differ, data-weighting schemes based on impedance tensor averages can lead to erroneous models, as the smaller impedance component(s) are effectively downweighted and information contained in these data may be lost. In addition, the inversion of data subsets, for example, single components, can provide instructive insights into the contribution of a particular component to the overall inversion result and may indicate structures, which are not or only poorly resolved by joint inversion.

Another important factor for the outcome of 3-D inversion is the set-up of starting and prior models. The ModEM3DMT inversion package, as many other codes, searches for the smallest deviation from the prior model, that is, the existence of an *a priori* model is inevitable. The resistivity level of the prior model prejudices the resistivity level of the inversion result. In presence of extended zones with strong resistivity contrasts, like in the SYNPRK model, this approach is prone to introduce artificial and misleading structures while substantial 2-D and 3-D structures are considerably compromised or suppressed. For the example from California, already intermediate background resistivity values for the prior or starting models causes the 3-D inversion to 'lose' the HCZ. Instead a spurious resistivity contrast (CC) appears beneath the coastline. Future version of ModEM should perhaps include a model regularization, which is more independent from a prior model.

The inclusion of *a priori* information, particularly on (elongated) zones with high-conductivity contrasts, even if outside of the station area, can have a stabilizing effect. The *a priori* insertion of high-resistive half-layers beneath the ocean was necessary to recover the true structure of the SYNPRK model, particularly the HCZ.

For a meaningful evaluation of the obtained inversion results, a systematic assessment of individual misfits and their variations in the frequency–space domain is essential. Results of both synthetic and field data inversions illustrate that the total rms is not a reliable measure to judge the quality of an inversion outcome. Models with similarly good rms values showed significantly differing and partly erroneous and misleading pictures of the subsurface. The quality of individual inversion results could only be assessed if data misfits were analysed separately for all inverted quantities. Such a systematic assessment of individual misfits is particularly useful to detect large-scale structural inconsistencies.

Moreover systematic differences in data-fit quality and differing misfit levels between single components can hint at more general challenges for the 3-D inversion approach. For both the California and the synthetic data, a systematic increase of long-period *yx*-impedance misfits towards the coastline hinted at insufficiently reproduced extended zones of high resistivity beneath the ocean, which impaired and partly inhibited recovery of the HCZ at depth. If a particular component cannot be fit, structural information contained in other components may be attenuated or even lost. In these cases, downweighting of consistently poorer-fitted data, for example, the *yx*-impedances of the SYNPRK data set, can improve resolution for information contained in other data or impedance components (*cf.* Fig. 10d).

If handled with necessary care, 3-D inversion of large real-world data sets is possible and rewarding. The extensive MT data from California could be inverted, mostly with excellent data fit. The 3-D conductivity models reveal structures to depths of approximately 60 km which are largely consistent with previous 2-D inversion results. In addition, 3-D inversion revealed new structures in the southern part of the survey area, where strong 3-D effects are present in the data. A number of 3-D structures with spatial continuity associated with sediments and mountain ranges appear in the upper 5 km. In this region the data fit of the 3-D model is significantly better than for 2-D.

In the 3-D models, the HCZ is imaged narrower and appears at shallower depth compared to 2-D. Inversion tests with synthetic data, however, indicate that 3-D inversion tends to place structures systematically at shallower depth levels than their true locations, if prior and starting models have (too) low resistivity. The 2-D results may have implied a continuous HCZ along strike but this could only be verified with 3-D inversion. The CP between the deep low-resistive zone and the upper crustal SAF, which was a robust feature in 2-D inversions of the northern profiles 2 and 3, could not be resolved with 3-D inversion. Its presence, however, is consistent with the data. Systematic tests with synthetic data (SYNPRK-path) indicate that the strong regularization required in 3-D inversion works against this feature.

We conclude that 2-D and 3-D inversion techniques should be used complementarily. 3-D inversion can be used to interpret large real-world data sets and has clear advantages over 2-D inversion approaches in complex subsurface situations. However, 2-D inversion provides still more options and control about the resolution of small-scale structures, as well as other aspects which have not been discussed here, e.g. the handling of static shift and the integration of topography and detailed bathymetry, as a much finer discretization of the subsurface can be realized.

As 3-D MT inversion is strongly ill-posed, inversion parameters should be systematically investigated. Appropriate choices for model and data parameters are interrelated and specific for each data set. Even for full 3-D inversion thorough analysis of dimensionality and strike behaviour of the data set is advisable. In presence of a pronounced geo-electric strike direction, a rotation of data and model grid should be considered. If the coordinate system is not aligned with a dominant strike direction, the outcome of 3-D inversion can be erroneous and misleading. A sensible data-weighting scheme is essential to recover the full information of all inverted components. If the inversion scheme penalizes deviations from a prior model, the set-up of the prior model has to be handled carefully and a range of prior models should be tested.

ACKNOWLEDGEMENTS

We would like to express sincere thanks to Michael Becken for detailed discussion of the 2-D results and providing the processed data. Gary Egbert kindly made his code available to us. Naser Meqbel greatly helped with innumerable discussions and getting 3-D inversion started. Ute Weckmann is thanked for constructive comments. Gary Egbert (editor), Paul Bedrosian and an anonymous reviewer made very helpful suggestions that contributed to a substantial improvement of the manuscript. The instruments for the experiments were provided by the Geophysical Instrument Pool Potsdam (GIPP). The field campaigns were funded by the Deutsche Forschungsgemeinschaft (DFG) and the German Research Centre for Geosciences Potsdam (GFZ). This work was funded by the Deutsche Forschungsgemeinschaft (Ri 1127/2, 4). Seismicity data are taken from the catalogue provided by the Northern California Earthquake Data Center (http://www.ncedc.org) and compiled by the Northern California Seismic Network, US Geological Survey, Menlo Park and the Berkeley Seismological Laboratory, University of California, Berkeley. Fault zone locations are from the California Geological Survey, Geologic Data Map Series No. 6.

REFERENCES

Árnason, K., Eysteinsson, H. & Hersir, G.P., 2010. Joint 1D inversion of TEM and MT data and 3D inversion of MT data in the Hengill area, SW Iceland, *Geothermics,* **39,** 13–34.

Avdeev, D. & Avdeeva, A., 2009. 3D magnetotelluric inversion using a limited-memory quasi-Newton optimization, *Geophysics,* **74,** F45–F57.

Becken, M., Ritter, O. & Burkhardt, H., 2008a. Mode separation of magnetotelluric responses in three-dimensional environments, *Geophys. J. Int.,* **172,** 67–86.

Becken, M., Ritter, O., Park, S.K., Bedrosian, P.A., Weckmann, U. & Weber, M., 2008b. A deep crustal fluid channel into the San Andreas Fault system near Parkfield, California, *Geophys. J. Int.,* **173,** 718–732.

Becken, M., Ritter, O., Bedrosian, P.A. & Weckmann, U., 2011. Correlation between deep fluids, tremor and creep along the central San Andreas fault, *Nature,* **480,** 87–90.

Bedrosian, P.A., 2007. MT+, integrating magnetotellurics to determine Earth structure, physical state, and processes, *Surv. Geophys.,* **28,** 121–167.

Bertrand, E.A. *et al.*, 2012a. Magnetotelluric imaging of upper-crustal convection plumes beneath the Taupo Volcanic Zone, New Zealand, *Geophys. Res. Lett.,* **39,** L02304, doi:10.1029/2011GL050177.

Bertrand, E.A. *et al.*, 2012b. Magnetotelluric imaging beneath the Taiwan orogen: an arc-continent collision, *J. geophys. Res.,* **117,** B01402, doi:10.1029/2011JB008688.

Caldwell, T.G., Bibby, H.M. & Brown, C., 2004. The magnetotelluric phase tensor, *Geophys. J. Int.,* **158,** 457–469.

Cumming, W. & Mackie, R., 2010. Resistivity imaging of geothermal resources using 1D, 2D and 3D MT inversion and TDEM static shift correction illustrated by a glass mountain case history, in *Proceedings World Geothermal Congress 2010,* Bali, Indonesia.

Egbert, G.D., 1997. Robust multiple-station magnetotelluric data processing, *Geophys. J. Int.,* **130,** 475–496.

Egbert, G.D. & Booker, J.R., 1986. Robust estimation of geomagnetic transfer functions, *Geophys. J. R. astr. Soc.,* **87,** 173–194.

Egbert, G.D. & Kelbert, A., 2012. Computational recipes for electromagnetic inverse problems, *Geophys. J. Int.,* **189**(1), 251–267.

Farquharson, C.G. & Craven, J.A., 2009. Three-dimensional inversion of magnetotelluric data for mineral exploration: an example from the McArthur River uranium deposit, Saskatchewan, Canada, *J. appl. Geophys.,* **68,** 450–458.

Farquharson, C.G., Oldenburg, D.W., Haber, E. & Shekhtman, R., 2002. An algorithm for the three-dimensional inversion of magnetotelluric data, in *Proceedings of the 72nd Annual International Meeting,* SEG, Expanded Abstracts, pp. 649–652.

Han, N., Nam, M.J., Kim, H.J., Lee, T.J., Song, Y. & Suh, J.H., 2008. Efficient three-dimensional inversion of magnetotelluric data using approximate sensitivities, *Geophys. J. Int.,* **175,** 477–485.

He, Z., Hu, Z., Luo, W. & Wang, C., 2010. Case history, mapping reservoirs based on resistivity and induced polarization derived from continuous 3D magnetotelluric profiling: case study from Qaidam Basin, China, *Geophysics,* **75,** B25–B33.

Heise, W., Caldwell, T.G., Bibby, H.M. & Bannister, S.C., 2008. Three-dimensional modelling of magnetotelluric data from the Rotokawa geothermal field, Taupo Volcanic Zone, New Zealand, *Geophys. J. Int.,* **173,** 740–750.

Heise, W., Caldwell, T.G., Bibby, H.M. & Bennie, S.L., 2010. Three-dimensional electrical resistivity image of magma beneath an active continental rift, Taupo Volcanic Zone, New Zealand, *Geophys. Res. Lett.,* **37,** L10301, doi:10.1029/2010GL043110.

Hill, G.J., Caldwell, T.G., Heise, W., Chertkoff, D.G., Bibby, H.M., Burgess, M.K., Cull, J.P. & Cas, R.A., 2009. Distribution of melt beneath Mount St Helens and Mount Adams inferred from magnetotelluric data, *Nat. Geosci.,* **2,** 785–789.

Ingham, M.R. *et al.*, 2009. A magnetotelluric study of Mount Ruapehu volcano, New Zealand, *Geophys. J. Int.,* **179,** 887–904.

Kelbert, A., Egbert, G.D. & deGroot Hedlin, C., 2012. Crust and upper mantle electrical conductivity beneath the Yellowstone Hotspot Track, *Geology,* **40**(5), 447–450.

Mackie, R.L., Smith, J.T. & Madden, T.R., 1994. Three-dimensional electromagnetic modeling using finite difference equations: the magnetotelluric example, *Radio Sci.,* **29,** 923–935.

Mackie, R.L., Madden, T.R. & Park, S., 1996. A three-dimensional magnetotelluric investigation of the California Basin and Range, *J. geophys. Res.,* **101**(B7), 16 211–16 239.

Mackie, R.L., Rodi, W. & Watts, M.D., 2001. 3-D magnetotelluric inversion for resource exploration, in *Proceedings of the 71st Annual International Meeting,* SEG, Expanded Abstracts, pp. 1501–1504.

Meqbel, N., 2009. The electrical conductivity structure of the Dead Sea Basin derived from 2D and 3D inversion of magnetotelluric data, *PhD thesis,* Free University of Berlin, Berlin, Germany.

Nadeau, R.M. & Dolenc, D., 2005. Nonvolcanic tremors deep beneath the San Andreas Fault, *Science,* **307,** 389.

Newman, G.A. & Alumbaugh, D.L., 2000. Three-dimensional magnetotelluric inversion using non-linear conjugate gradients, *Geophys. J. Int.,* **140,** 410–424.

Newman, G.A., Gasperikova, E., Hoversten, G.M. & Wannamaker, P.E., 2008. Three-dimensional magnetotelluric characterization of the Coso geothermal field, *Geothermics,* **37,** 369–399.

Page, B.M., Thompson, G.A. & Coleman, R.G., 1998. Late Cenozoic tectonics of the central and southern Coast Ranges of California, *Geol. Soc. Am. Bull.,* **110,** 846–876.

Patro, P.K. & Egbert, G.D., 2008. Regional conductivity structure of Cascadia: preliminary results from 3D inversion of USArray transportable

array magnetotelluric data, *Geophys. Res. Lett.,* **35,** L20311, doi:10.1029/2008GL035326.

Patro, P.K. & Egbert, G.D., 2011. Application of 3D inversion to magnetotelluric profile data from the Deccan Volcanic Province of Western India, *Phys. Earth planet. Inter.,* **187,** 33–46.

Ritter, O., Junge, A. & Dawes, G., 1998. New equipment and processing for magnetotelluric remote reference observations, *Geophys. J. Int.,* **132,** 535–548.

Rodi, W. & Mackie, R.L., 2001. Nonlinear conjugate gradients algorithm for 2-D magnetotelluric inversion, *Geophysics,* **66,** 174–187.

Ryberg, T., Haberland, C., Fuis, G.S., Ellsworth, W.L. & Shelly, D.R., 2010. Locating non-volcanic tremor along the San Andreas Fault using a multiple array source imaging technique, *Geophys. J. Int.,* **183,** 1485–1500.

Sasaki, Y., 2001. Full 3-D inversion of electromagnetic data on PC, *J appl. Geophys.,* **46,** 45–54.

Shelly, D.R., 2010. Migrating tremors illuminate complex deformation beneath the seismogenic San Andreas fault, *Nature,* **463,** 648–652.

Shelly, D.R. & Hardebeck, J.L., 2010. Precise tremor source locations and amplitude variations along the lower crustal central San Andreas Fault, *Geophys. Res. Lett.,* **37,** L14301, doi:10.1029/2010GL043672.

Shelly, D.R., Ellsworth, W.L., Ryberg, T., Haberland, C., Fuis, G.S., Murphy, J., Nadeau, R.M. & Burgmann, R., 2009. Precise location of San Andreas Fault tremors near Cholame, California using seismometer clusters: slip on the deep extension of the fault? *Geophys. Res. Lett.,* **36,** L01303, doi:10.1029/2008GL036367.

Siripunvaraporn, W. & Egbert, G., 2000. An efficient data-subspace inversion method for 2D magnetotelluric data *Geophysics,* **65,** 791–803.

Siripunvaraporn, W. & Egbert, G., 2009. WSINV3DMT: vertical magnetic field transfer function inversion and parallel implementation, *Phys. Earth planet. Inter.,* **173,** 317–329.

Siripunvaraporn, W., Egbert, G., Lenbury, Y. & Uyeshima, M., 2005. Three-dimensional magnetotelluric inversion: data-space method, *Phys. Earth planet. Inter.,* **150,** 3–14.

Tuncer, V., Unsworth, M.J., Siripunvaraporn, W. & Craven, J.A., 2006. Exploration for unconformity-type uranium deposits with audiomagnetotelluric data: a case study from the McArthur River mine, Saskatchewan, Canada, *Geophysics,* **71**(6), B201–B209.

Türkoğlu, E., Unsworth, M. & Pana, D., 2009. Deep electrical structure of northern Alberta (Canada): implications for diamond exploration, *Can. J. Earth Sci.,* **46,** 139–154.

Weckmann, U., Magunia, A. & Ritter, O., 2005. Effective noise separation for magnetotelluric single site data processing using a frequency domain selection scheme, *Geophys. J. Int.,* **169,** 635–652.

Xiao, Q., Cai, X., Xu, X., Liang, G. & Zhang, B., 2010. Application of the 3D magnetotelluric inversion code in a geologically complex area, *Geophys. Prospec.,* **58,** 1177–1192.

Zhang, H., Nadeau, R.M. & Toksoz, M.N., 2010. Locating non-volcanic tremors beneath the San Andreas Fault using a station-pair double-difference location method, *Geophys. Res. Lett.,* **37,** L13304, doi:10.1029/2010GL043577.

Zhdanov, M.S., Fang, S. & Hursán, G., 2000. Electromagnetic inversion using quasi-linear approximation, *Geophysics,* **65,** 1501–1513.

Zhdanov, M.S., Green, A., Gribenko, A. & Cuma, M., 2010. Large-scale three-dimensional inversion of EarthScope MT data using the integral equation method, *Phys. Solid Earth,* **46,** 670–678.